Materials & Design 244 (2024) 113122

Contents lists available at ScienceDirect

Materials & Design

journal homepage: www.elsevier.com/locate/matdes

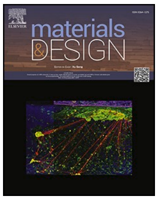

Fatigue crack initiation and propagation in plain and notched PBF-LB/M, WAAM, and wrought 316L stainless steel specimens

Moritz Braun [a,b,*], Ting Chen [c], Junjun Shen [c], Henrik Fassmer [b], Benjamin Klusemann [c,d], Shahram Sheikhi [e], Sören Ehlers [a,b], Eckehard Müller [f,g], Ardeshir Sarmast [h], Jan Schubnell [h]

[a] German Aerospace Center (DLR), Institute of Maritime Energy Systems, Geesthacht, Germany
[b] Hamburg University of Technology, Institute for Ship Structural Design and Analysis, Hamburg, Germany
[c] Helmholtz-Zentrum Hereon, Institute of Material and Process Design, Solid State Materials Processing, Geesthacht, Germany
[d] Leuphana University Lüneburg, Institute for Production Technology and Systems, Lüneburg, Germany
[e] University of Applied Science Hamburg, Institute of Materials Science and Joining Technology, Hamburg, Germany
[f] Bochum University of Applied Sciences, Department of Mechatronics and Mechanical Engineering, Bochum, Germany
[g] Steinbeis-Transfercenter for Spring Technologies, Component Behavior and Process, Iserlohn, Germany
[h] Fraunhofer Institute for Mechanics of Materials IWM, Freiburg, Germany

ARTICLE INFO

Keywords:
Hybrid additive manufacturing
Selective laser melting
Wire arc additive manufacturing
Microstructural defects
Post-production treatment
Fatigue strength assessment

ABSTRACT

Additively manufactured (AM) components—either made by laser-powder bed fusion or wire and arc additive manufacturing—typically contain process-related defects on and near surfaces that can be removed by machining. Various studies have shown that post-treatment, such as machining significantly improves the fatigue strength of AM parts. To this day, however, hardly any studies have investigated the fatigue strength of post-treated additively manufactured components with notches. In this study, fatigue tests were performed on plain and notched specimens to determine and compare the crack initiation and crack propagation behavior due to different manufacturing-related effects. Tests were performed on specimens produced by the two aforementioned AM processes and compared to specimens taken from wrought sheets. The fatigue strength of AM materials is influenced by microstructure, defects, residual stress, and notches. PBF-LB/M specimens exhibit the highest fatigue strength in plain, notch-free conditions, attributed to differences in microstructure and static strength affecting fatigue crack initiation. Notched specimens show larger differences among materials, with PBF-LB/M having shorter fatigue crack propagation life related to line-type defect clusters, while the plain PBF-LB/M specimens are less affected as their fatigue strength is primarily determined by fatigue crack initiation.

1. Introduction

In recent years, additive manufacturing (AM) has gained a lot of interest in manufacturing due to unparalleled design freedom and customization in the production of metallic components. Laser-Based Powder Bed Fusion of metals (PBF-LB/M) and Directed Energy Deposition (DED) techniques, such as Wire and Arc Additive Manufacturing (WAAM), are two prominent AM techniques that have gained widespread attention due to their unique capabilities in creating complex structures; however, in some cases, AM components have very different mechanical properties after production compared to conventional semi-finished products [1]. In contrast to semi-finished products, pores and other defects, as well as rough surfaces (see Fig. 1) and introduced tensile residual stresses, lead to lower fatigue strength of AM parts and components [2]. In addition, the manufacturing process determines the specific microstructure-property relationship. Parts made from the same alloy but manufactured by different processes typically show distinct differences in microstructure and thereby in mechanical properties [3]. Thus, differences in mechanical properties between different AM and conventional manufacturing processes are linked to a complex interaction between microstructure, defects, surface conditions, and residual stress states.

Despite the design freedom, AM parts often still contain notches, e.g., due to branched designs or for holes for bolts or rivets etc. At notches, the fatigue performance of AM parts is often reduced by unfavorable mechanics such as stair-stepping and accumulation of defects [5]. Post-

---

* Corresponding author at: German Aerospace Center (DLR), Institute of Maritime Energy Systems, Geesthacht, Germany.
E-mail address: moritz.braun@dlr.de (M. Braun).

https://doi.org/10.1016/j.matdes.2024.113122
Received 25 March 2024; Received in revised form 16 June 2024; Accepted 25 June 2024

treatment is a useful approach to improve the fatigue strength of AM components, see [6]. Post-treatment techniques can be categorized into surface treatment [7], residual stress state altering techniques [8], or combinations of both [9]. Surface treatment by machining (e.g., milling, grinding, turning, or polishing) is an inexpensive and effective approach to reduce surface roughness and to remove surface at near-surface effects, especially for stainless steels. A comprehensive comparison of 21 different surface and hybrid treatment methods has recently been published by Maleki and Shamsaei [10]. To the authors knowledge, studies on post-treated AM parts by machining focus almost exclusively on plain specimens without notches; however, notches are typically more critical locations from a fatigue perspective. In addition, a comparison of the effect of machining on stainless steels AM parts produced by different processes has not yet been performed. Thus, a comprehensive understanding of the fatigue performance of machined stainless steel AM components manufactured through different processes is crucial for ensuring their structural integrity.

This study addresses two important questions. 1) How does the fatigue strength of machined 316L additively manufactured components produced by PBF-LB/M and WAAM compare to components made from conventional hot-rolled sheet material in plain and notched state. 2) How do microstructural and mechanical properties, as well as macro geometric notches influence the fatigue crack initiation and propagation behavior of AM and wrought components?

The study delves into the influence of notches on the fatigue strength of these components, recognizing the significance of geometric features in actual applications where stress concentrations are unavoidable. The study takes into account the distinct microstructural and mechanical characteristics associated with the PBF-LB/M and WAAM processes, as well as the inherent material differences between additively manufactured parts and their conventionally produced counterparts. In this regard, experimental investigations are conducted utilizing fatigue testing, incorporating two notch configurations and plain specimens without notches. The results obtained are expected to provide valuable insights into the comparative fatigue performance of PBF-LB/M and WAAM components, shed light on the role of notches in influencing their structural integrity.

2. Influencing factors on fatigue strength of surface treated additively manufactured components

2.1. Microstructure

Theoretically, under equal conditions, the fatigue crack-initiation is favored in coarse-grained materials when compared to fine-grained materials. Thus, a decrease in grain size in microcrystalline materials, leads to an increase in fatigue crack initiation life, while at the same time reduces crack propagation life [11]. In polycrystalline metallic materials with high surface quality that lack internal imperfections, the initiation of cracks is typically propelled by slip bands [12]. In broad terms, microstructures characterized by finer features exhibit enhanced resistance to crack initiation compared to coarser counterparts, due to a heightened density of slip bands. In addition, the initiation of fatigue cracks in textured materials is influenced by the orientation of the active slip system(s) in relation to the loading direction(s); however, also the crystallographic orientations of adjacent grains influences early fatigue crack growth [2]. For instance, high-angle grain boundaries (HAGBs) are known to hinder fatigue crack propagation [13].

The microstructure of additively manufactured components—particularly those fabricated through PBF-LB/M and WAAM—significantly affects their fatigue strength compared to conventionally manufactured components made from wrought material. In PBF-LB/M, rapid solidification rates during the layer-by-layer deposition process can often result in non-equilibrium microstructures with irregular grain morphologies and anisotropic material properties. Such microstructures affect the fatigue performance and failure mechanism of the part, especially pertaining to crack initiation and short crack growth [2]. In addition, PBF-LB/M microstructure frequently feature small defects such as pores or unmelted powder. For example, pores may arise at the start or stop positions of the scanning pattern due to changes in heat input, see Huang et al. [14] and Cunningham et al. [15].

On the other hand, WAAM—which involves layer-wise welding—induces thermal cycles leading to a distinct microstructural evolution with large columnar grains. Such microstructure results in lower strength, toughness, and corrosion resistance compared to a fine equiaxed microstructure [16]. The presence of fine equiaxed grains mitigates solidification cracking while enhancing the material's toughness, ductility, and strength [17]. The presence of columnar grains and epitaxial growth can create preferential paths for crack initiation, while the non-equilibrium phases may introduce inherent material heterogeneities affecting crack growth rates [18].

In contrast, conventionally manufactured components from hot-rolled stainless steel possess a coarse microstructure, influenced by the thermomechanical processing involved in their production. The hot rolling process involves heating the stainless steel billet or slab to high temperatures and then passing it through a series of rollers to reduce its thickness and shape it into the desired form. During this hot deformation, recrystallization and grain growth occur, resulting in the formation of larger and irregularly shaped grains. This inherent microstructure may exhibit preferential crack initiation sites and reduced fatigue resistance; however, a more regular microstructure is achieved through an additional annealing process yielding a microstructure with equiaxed grains.

The microstructures in PBF-LB/M 316L samples typically consist of irregular grains ranging from 1 to 500 μm in size, with serrated and wavy grain boundaries. It is further characterized by a relatively high density of lattice dislocations of about 5×10^{14} m^{-2}, which are organized into a uniform dislocation cell substructure [19]. It has been acknowledged that this dislocation cell substructure plays a pivotal role in enhancing the strength of austenitic stainless steels achieved through

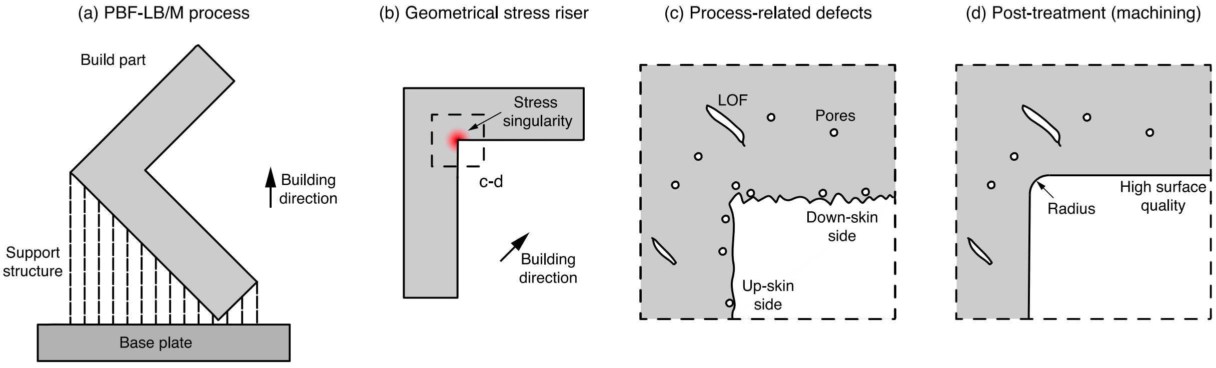

Fig. 1. Schematic illustration of the PBF-LB/M process and implications of post-treatment by machining on AM parts produced; based on [4].

PBF-LB/M [20]. Wang et al. [21] reported that WAAM 316L revealed intricate microstructures with multiple layers, evident in both the building and transverse orientations. Along the building direction, grains exhibited epitaxial growth, accompanied by periodic alterations in ferrite morphology. In the transverse direction, two distinct microstructural regions emerged: the remelting area (RA) and the overlapping area (OA). The RA, characterized by grains growing perpendicular to the fusion lines, featured finer columnar grains and a higher proportion of HAGBs. Conversely, the OA, where grains grew along the building direction, presented large-sized directional growth grains with a distinct texture. In general, higher deposition rates or heat input may lead to low cooling rates, and hence to unfavorable microstructure and component properties, but at the same time, yields lower tensile residual stress levels [22].

In contrast in rolled and annealed steel, the evolution of ultra-fine grain microstructures occurs through the annealing process, involving austenite reversal in the rolled material, coupled with successive stages of continuous recrystallization and grain growth [23]. These microstructures exhibited a refined grain size of approximately 0.5 μm and a dislocation density of about 10^{15} m^{-2} following annealing at 973 K for hot-rolled 316L type steel [24].

In summary, the influence of microstructure on fatigue strength is a critical parameter for the comprehensive assessment and comparison of the structural integrity of 316L stainless steel components produced through different manufacturing techniques.

2.2. Residual stress state

Both fatigue crack initiation and propagation are known to be influenced by residual stresses. Tensile residual stresses are well-known to reduce fatigue strength of any structural component, while compressive residual stresses increase the fatigue strength; however, production-related residual stresses are often partially released during cyclic loading [25].

The residual stresses in PBF-LB/M and WAAM components made from 316L steel are significant different from those in conventional hot-rolled and annealed steel. In PBF-LB/M and WAAM, the rapid heating and cooling cycles during the additive manufacturing process introduce complex thermal gradients, leading to residual stresses that are inherent to the layer-wise deposition [26,27]. These additive manufacturing techniques often result in higher levels of residual stresses compared to conventionally produced hot rolled and annealed steel due to the localized melting and solidification, inherent in the layer-by-layer build-up of the material.

Several investigations on 316L but also other steels show high tensile residual stresses in the upper layer of the PBF-LB/M parts and compressive residual stresses in lower layers, see e.g., [28,29]. In both PBF-LB/M and WAAM components, the residual stresses are found to be dependent on the building/deposition direction. In addition, the constraint of the build plates influences the build-up residual stresses, but their removal also leads to a partial residual stress release [30].

In summary, the influence of residual stresses on the structural integrity of AM parts is substantial. High residual stresses influence fatigue performance, crack initiation, and propagation, thereby affecting the overall structural integrity of the additively manufactured parts. Consequently, understanding and mitigating residual stresses is crucial for the structural integrity of PBF-LB/M and WAAM components. Thus, this study investigates the effect of microstructure and residual stresses on fatigue crack initiation and propagation of AM components with notches made by different processes and compares it to conventionally fabricated parts from hot-rolled and annealed steel.

3. Material and specimen fabrication

AISI 316L (X2CrNiMo17-12-2, 1.4404) is investigated, representing an austenitic stainless steel characterized by excellent mechanical properties, as well as high corrosion resistance [31]; however, it is difficult to machine [32]. The chemical composition of the employed powder is listed in Table 1.

To investigate the effect of AM processes on notched components, two sets of specimens with different notch acuity were fatigue tested and compared to plain specimens without a notch. The U-notched specimens are characterized by a notch opening angle of $\omega = 0^\circ$, while the V-notched specimens have a notch opening angle of $\omega = 135^\circ$. An overview of the general dimensions of the specimens is shown in Fig. 2. Both types of specimens have a thickness of 4 mm and thus a nominal cross-sectional area of 24 mm^2. The reason for the small size of the specimens is due to the goal of testing specimens with realistic dimensions that represent both relatively mild and sharp notch geometries. In addition, the notched specimens have a large radial cutout on the opposite site to make sure that the cracks start on one side with the notches. This enables a reliable monitoring of crack initiation and propagation behavior. The depth of the notches and the cutouts are identical to prevent secondary bending of the specimens.

The stress concentration factors for both specimens—determined by finite element simulations—are $K_t = 1.87$ for the U-notched and $K_t = 5.75$ for the V-notched specimens. Due to the machining difficulties of 316L, specimens with small oversizes were manufactured from the different deposited structures as well as plate material. All specimens were fabricated with an oversize of 1 mm on all surfaces, which was later removed by machining and wire erosion, resulting in all specimens having the same final dimension.

The PBF-LB/M specimens (see Fig. 3(a)) were produced in a Renishaw AM250 PBF-LB/M machine in the vertical direction onto a 316L base plate with 13.6 mm thickness and 248 mm length and width. The U-type specimen required a support structure for the overhang, which was later removed manually. The employed process parameters are summarized in Table 2. The PBF-LB/M specimens were all subjected to heat treatment at 650 °C for 2 h in an oven. The temperature and duration were chosen based on two other studies on the same material [33,34]. The z-direction refers to the building direction and the welding direction for the PBF-LB/M and WAAM specimens, respectively.

Additional specimens were fabricated using the WAAM process, see Fig. 3(b). WAAM is based on gas-shielded metal arc welding and enables a fast fabrication of larger voluminal than PBF-LB/M. For the WAAM process, a welding wire (1.2 mm diameter) with the same chemical composition as the powder of the PBF-LB/M specimens and a conventional shielding gas (82 % argon and 12 % CO2) were used. The nozzle distance was 12 mm. The equipment consists of a Fronius power source and a gantry system as a handling system for the CMT (Cold Metal Transfer) process. The CMT process ensures a uniform and continuous droplet transfer. The process parameters are summarized in Table 3. For the WAAM process, the characteristic curve was provided by the equipment manufacturer EES Schweißtechnik and the individual voltage and current values were chosen based on pretests. The L-PBF parameters were optimized in previous studies, see, e.g., Braun et al., [35]. The WAAM specimens were tested without heat treatment.

The last type of specimens, intended to reflect conventional manufacturing processes based on wrought material, were taken from a 4 mm thick hot-rolled and annealed sheet and has a similar tensile strength to the specimens produced using by PBF-LB/M process, see [35].

Table 1
Chemical composition of 316L used for fabrication of PBF-LB/M specimens.

	C	Mo	Ni	Ma	Cr	Si	O	Fe
Weight (%)	0.006	2.5	12.5	1.5	16.6	0.7	0.063	Balanced

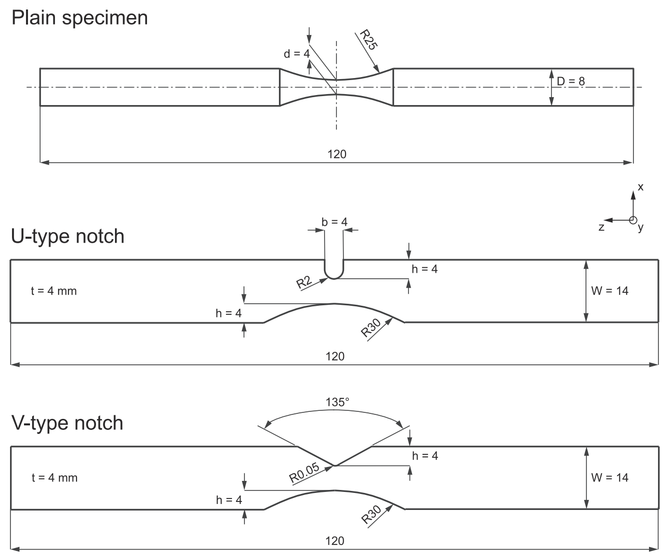

Fig. 2. Schematic illustration of specimen geometries.

4. Specimen and material characterization

4.1. Microstructure and material characterization

Examples of as-manufactured PBF-LB/M and WAAM specimens were examined using CT scans. For this purpose, a PBF-LB/M specimen before machining with intact support structure was selected. The scan was performed using a Yxlon FF35 CT scanner with a voxel size of about 11.9 μm. A number of defects were found near the plane with the smallest cross-sectional area of the U-notched specimens (marked in Fig. 4(a)). These defects may affect fatigue crack growth due to their location. In contrast, the WAAM specimens contained only minor defects compared to the PBF-LB/M specimen, see Fig. 4(b).

In addition to the CT scan, micrographs of the PBF-LB/M 316L for the smallest cross-sections, i.e., the plane (x-y), where a number of defects were observed in the CT scan, were created, see Fig. 5. Comparing the etched and non-etched micrographs it becomes evident that the line-type defect clusters of the pores are aligned with the scanning pattern of the PBF-LB/M process, i.e., a rotation of the scanning pattern of 67°. Each defect is individually rather small and on average more than two times its diameter away from each other; however, the fact that the defects are in the same plane perpendicular to the loading direction can have a significant effect on the fatigue crack propagation behavior. Defects aligning with the scanning direction were also observed in other studies and does not seem to be coincidental, see Han et al. [36].

In addition, electron backscatter diffraction (EBSD) data were collected on an FEI Quanta 650 FEG scanning electron microscope equipped with a Velocity Super EBSD system. EBSD mapping was performed with an acceleration voltage of 25 kV and a step size of 0.5 μm. Each scan area was set to 699 × 547.8 μm^2.

Fig. 6 depicts the inverse pole figure (IPF) of 316L stainless steel in wrought alloy, PBF-LB/M, and WAAM, respectively, highlighting significant differences in grain shape and size among these materials. Wrought 316L stainless steel exhibits equiaxed grains and twins, with an average grain size of approximately 30 μm (see Fig. 6(a)-(c)). In contrast, PBF-LB/M 316L stainless steel showcases a bimodal microstructure featuring large columnar grains alongside fine equiaxed grains, with the columnar grains aligned parallel to the building direction (see Fig. 6(d)-(f)). WAAM 316L stainless steel consists of much larger columnar grains (see Fig. 6(g)-(i)), also aligned parallel to the travel direction, similar to PBF-LB/M 316L stainless steel. These grains are elongated almost in the whole thickness of the specimen, due to the dominant heat flow in this direction. Fig. 7 presents the pole figure (PF) of 316L stainless steel in wrought alloy, PBF-LB/M, and WAAM, reflecting grain orientation distributions. Wrought 316L stainless steel exhibits a typical face-centered cubic (fcc) structure texture (see Fig. 7(a)). In the PF of PBF-LB/M 316L stainless steel, a [1 1 0] pole peak is aligned with the building direction (see Fig. 7(b)), indicating a preferred orientation of the columnar grains (colored green in Fig. 6(f)) with $\langle 1\,1\,0 \rangle$ building direction. The PF of WAAM 316L stainless steel—characterized by large dendritic columnar

Table 2
Process parameters used for fabrication of the PBF-LB/M 316L specimens.

Laser power [W]	Layer thickness [μm]	Powder density [g/cm³]	Width of molten pool [μm]	Exposure time [μs]	Scan line spacing [μm]	Rotation of scan vector
100 – 180	40	4.29	115	80	65	67°

Table 3
Process parameters of the WAAM specimen production.

Layer	Wire feed speed [m/min]	Current [A]	Voltage [V]	Arc travel speed [mm/min]
1. Layer	5.4	107	19.2	800
2. Layer	4.6	89	19.0	800
3. to 8. Layer	4.0	78	17.6	680

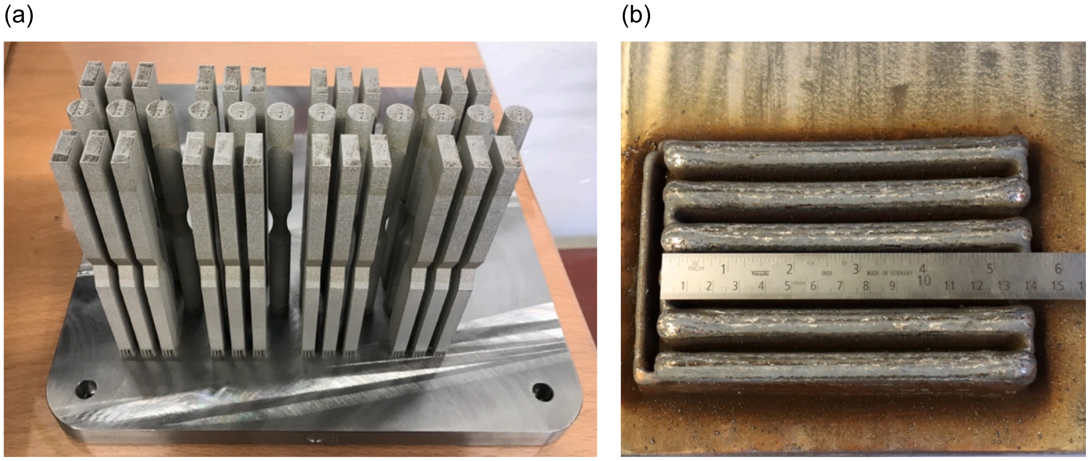

Fig. 3. Fabrication of PBF-LB/M (a) and WAAM (b) specimens.

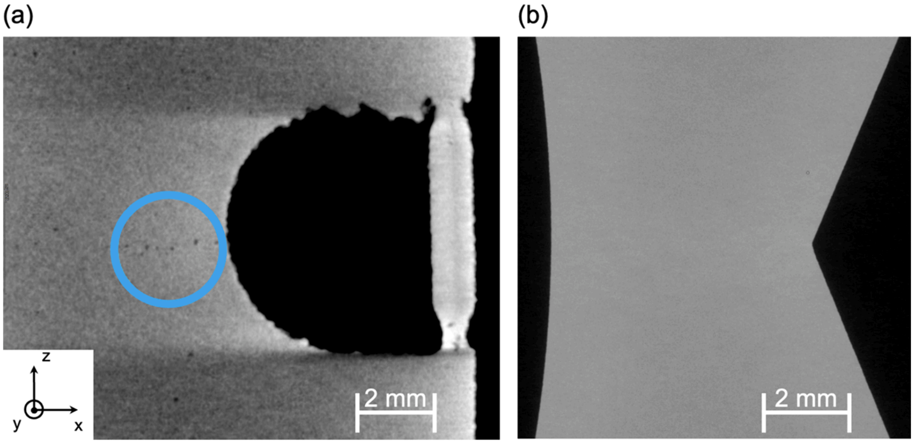

Fig. 4. CT scan of PBF-LB/M fabricated 316L specimen with U-notch and marking of defects lying in a plane perpendicular to the loading direction (a) and CT scan of WAAM specimen with V-notch (b).

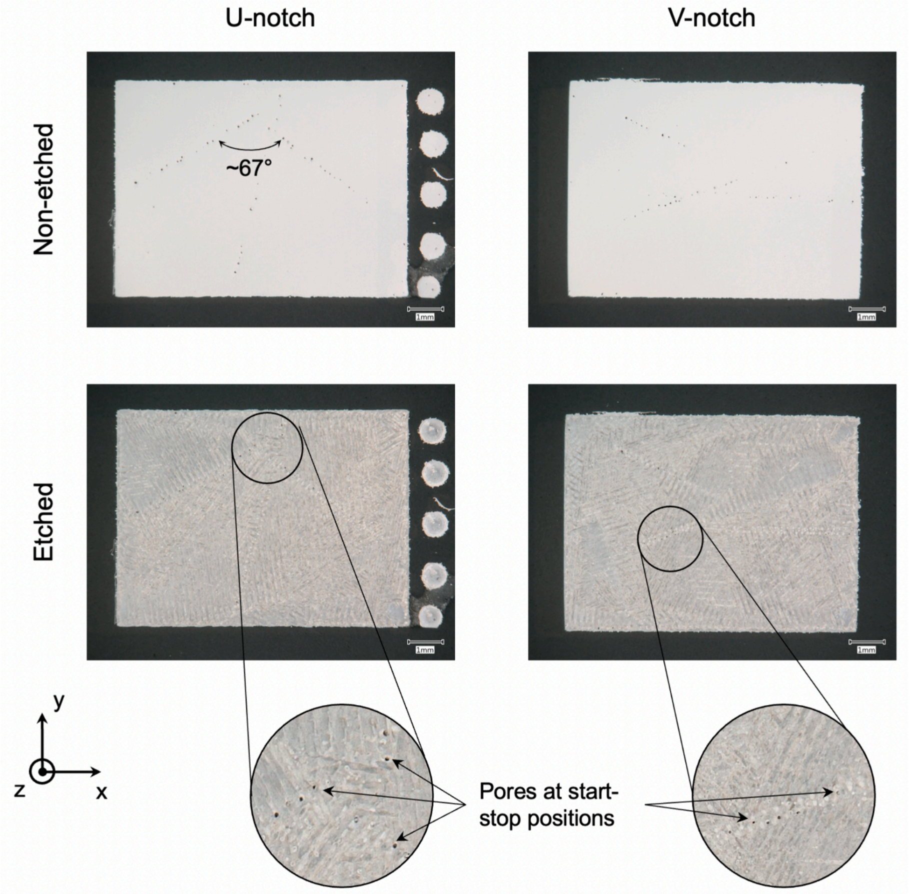

Fig. 5. Microstructure of PBF-LB/M 316L stainless steel in etched and non-etched state to highlight the line-type defect clusters of pores at start-stop positions.

grains—displays a strong [001] pole peak aligned with the welding direction (see Fig. 7(c)). A similar microstructure was also observed in 316L stainless steel produced by selective laser melting (SLM) using a high-power laser by Montero-Sistiaga et al. [37].

The difference between the microstructure of PBF-LB/M and WAAM 316L stainless steel could be attributed to the ratio of the temperature gradient (G) to the growth rate (R) of grains during solidification and different heat flow in the samples, see [16]. The temperature gradient G is the ratio of the temperature difference between the maximum temperature and fusion line temperature and the distances between these points ($G = {}^{\Delta T}/_{\Delta x}$). This gradient plays a crucial role in determining the microstructure, therefore, quality and properties of the manufactured part. Decreasing the G/R ratio changes the solidification microstructure within the grains from cellular to columnar dendritic and equiaxed dendritic structures. Smaller melt pool dimensions of the PBF-LB/M samples cause higher temperature gradients (G) and formation of columnar structures, as observed in Fig. 5. The different grain structure of the materials is mainly affected by the directional cooling of the specimens. During the solidification, the grains of the substrate or previously deposited layers act as the nuclei for the new grains. These newly

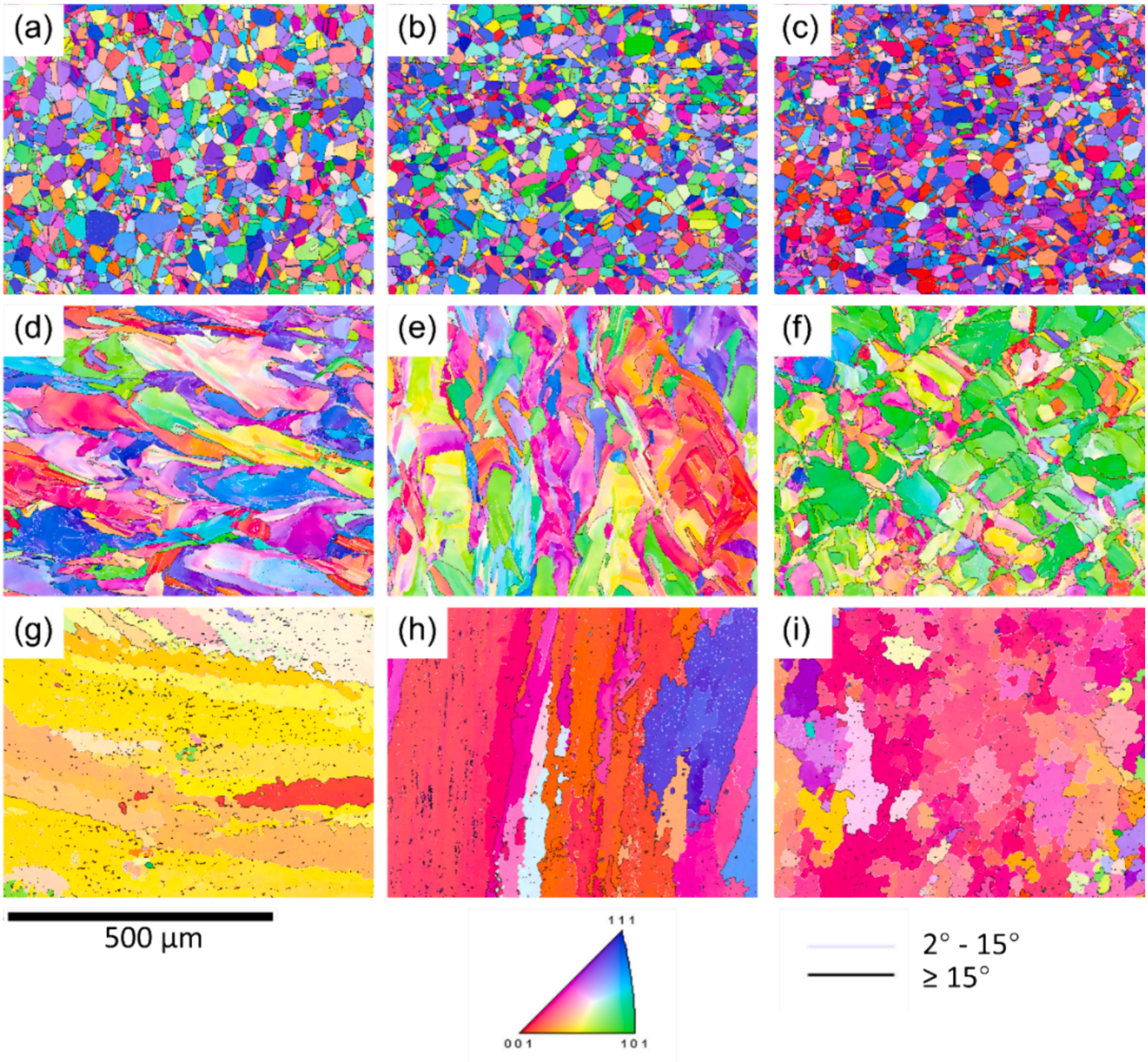

Fig. 6. Electron backscatter diffraction inverse pole figure with low angle grain boundary, marked by grey line, and high angle grain boundary, marked by black line, of 316L stainless steel: (a)-(c) wrought, (d)-(f) PBF-LB/M and (g)-(i) WAAM on different planes: (a),(d),(g) zx, (b),(e),(h) yz, and (c),(f),(i) xy.

formed grains grow in the direction of the maximum heat flow. When the heat flows almost uniformly throw the material in all three directions, large columnar grains, which form in case of one directional heat flow, are replaced by smaller irregular grains to form a polycrystalline-like microstructure, and consequently texture intensity decreases [38]. In the WAAM specimens, due to the large melt pool dimensions and the single-track geometry of the samples, heat mainly flows through the thickness (in the build direction), which results in the grain growth in this direction and formation of columnar grains, Fig. 6 (h). In the PBF-LB/M, on the other hand, due to the small size of the melt pool compared to the substrate, heat flows in all three directions resulting in more equiaxed grains, Fig. 6(d) and (e). Although, these grains are still courser than the wrought sample, due to the exposure of the PBF-LB/M sample to high temperatures. The microstructure transitions with change of G/R have also been reported by Gokcekaya et al. [39] and Ghayoor et al. [40] when they investigated the effects of laser power and scanning speed of PBF-LB/M and SLM.

4.2. Local hardness measurements

The micrographs of the PBF-LB/M notched specimens have shown pores at the start or stop positions of the scan pattern. This could be caused by changes in heat input, as the processing parameter for these locations may be outside of the optimal power-velocity processing parameter space. This may cause keyhole fluctuation and pore formation, see Huang et al. [14] and Cunningham et al. [15]. It is consequently often advised to adjust the power-velocity combination to control power density distribution and heat input [41].

In general, changes in heat input should in general also influence the static strength of the material [42]. Due to the correlation between the material strength and hardness such variations can be determined from hardness measurements. Thus, local hardness measurements were performed using a Struers DuraScan 70 instrument to determine if there were differences in hardness at the notch root area and the smallest cross section, where the pores were detected.

The results for the three materials are shown in Fig. 8. The hardness map of the PBF-LB/M material in Fig. 8(b) reveals that there are no significant differences in hardness between the small and wider cross sections of the specimen. This indicates that the differences in heat input were small. In addition, the results show that the hardness of the wrought and PBF-LB/M material are in a similar range, while the hardness of the WAAM specimens is significantly lower. This is evidently related to the high heat input during the WAAM process that yields an unfavorable microstructure with larger dendritic columnar grains.

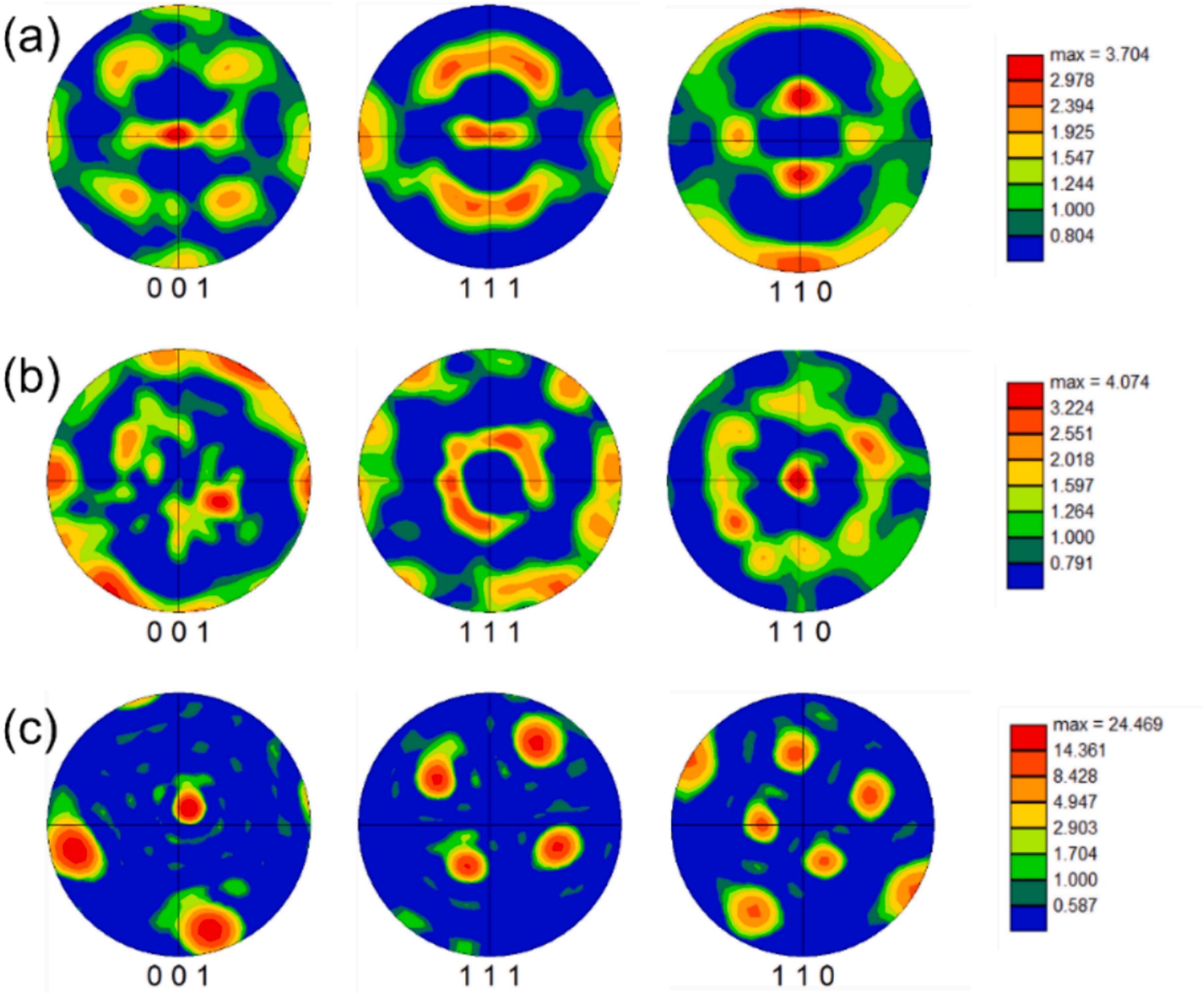

Fig. 7. Pole figure on xy plane of 316L stainless steel: (a) wrought, (b) PBF-LB/M and (c) WAAM.

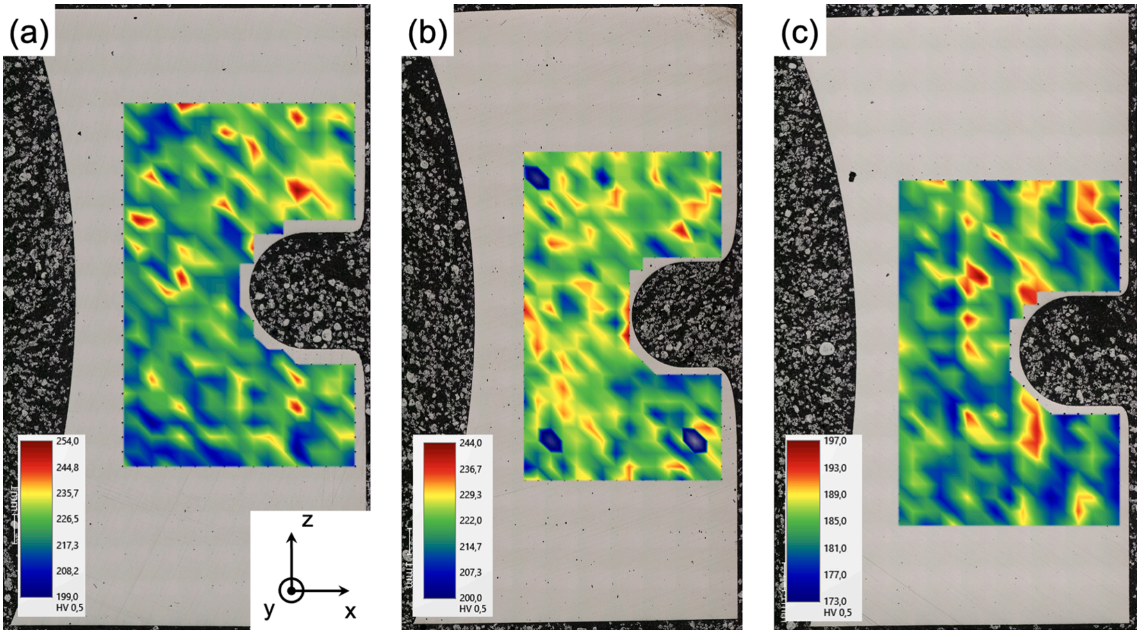

Fig. 8. Local hardness measurements of 316L stainless steel fabricated from (a) wrought, (b) PBF-LB/M and (c) WAAM material.

Although the hardness of the wrought and PBF-LB/M material are in a similar range, higher yield and ultimate tensile strength were observed for the PBF-LB/M compared to the wrought material, see [35]. The higher static strength can be attributed to multiscale microstructural features such as cellular dislocation substructures and bimodal grain size distribution [43]. Such effects are not captured by hardness measurements despite the low indentation force. Typically, higher static strength is beneficial for fatigue strength—in particular for specimens with smooth surfaces after machining.

4.3. Residual stress measurements

For all three materials, residual stresses were determined by X-ray diffraction (XRD) on a V-notched specimen using the $\sin^2\psi$ method. Measurements were performed along a path to the notch bisector and in addition, a depth profile was made in the middle of the notch bisector. Fig. 9 presents the measurement points along a path to the notch bisector.

WAAM parts usually contain coarse grains and a strong crystallographic texture [44], which negatively affect the accuracy of the XRD measurements. To obtain reliable measurements, the $\sin^2\psi$ method was applied with more tilt angles to increase the grain statistics. Measurements were performed using a stationary Bruker D8 Discover instrument with a Cr-K_α radiation ($\lambda = 2.2897$ Å) and a position sensitive detector (PSD). To reach a sufficient number of reflections for the XRD analysis, the measurement spot of 16x4.2 mm^2 (line focus) was used due the coarse grain microstructure of the WAAM specimen (Fig. 10). The samples were tilted from −57° to 57° for 30 angles. Due to the footprint effect of the *iso*-inclination setup at the utilized tilt angles, the beam height increases up to 7 times of the used slit height. Therefore, a 0.6 mm slit was used to avoid reflections from the sample holder or instrument parts besides the sample. The width of the slit was 16 mm. Fig. 12 shows the area (roughly 16x4.2 mm^2) of the sample covered by each measurement at 0° tilt angle. Furthermore, due the coarse grain microstructure of the WAAM specimen, see Fig. 6(g) – (i), a large measurement area is needed to reach a reliable grain statistics of reflection peaks in XRD analysis.

The (220) planes of the γ-Fe at $2\theta_0 = 128.8°$ were targeted and Young's modulus and Poisson's ratio were assumed to be 219 GPa and 0.29, respectively [25]. The in-house software StressIWM was used for the residual stress calculations. For more details on the underlying calculations, the interested reader is referred to [45]. Due to the geometry of the specimen, measurements were only performed in the transverse direction to the notch (x-direction in Fig. 10). It is worth mentioning in the iso-inclination geometry (line focus of the instrument), the tilting axis of rotation is parallel to the x-ray line (the red line in Fig. 10). Thus, the sample tilts perpendicular to the x-ray beam (red line in Fig. 10). Since the tilt direction determines the measurement direction, the residual stress is measured perpendicular to the x-ray line. In the longitudinal direction (z-direction in Fig. 10), the x-ray beam (the red line) will rotate 90°. Since the width of the notch is 6 mm, the area covered by the x-ray beam in this orientation is 6×4.2 mm^2. Due to the smaller scanning area compared to the transverse direction, most of the tilt angles did not show reflections with high enough intensities to give reliable results. Therefore, the measurement results in this direction were not further analyzed. To study the residual stress gradients in the depth and lateral directions, seven measurements were performed on the surface with 1 mm spacing in the vertical direction, and five measurements in the depth of the specimen in 60 µm steps between the first four points and 80 µm between the last measurement and the one before. The specimens were electropolished incrementally to remove the material from the surface. To include the effect of the material removal on the stress relief of the specimen, the following correction equation suggested by Sikarskie [46] was used:

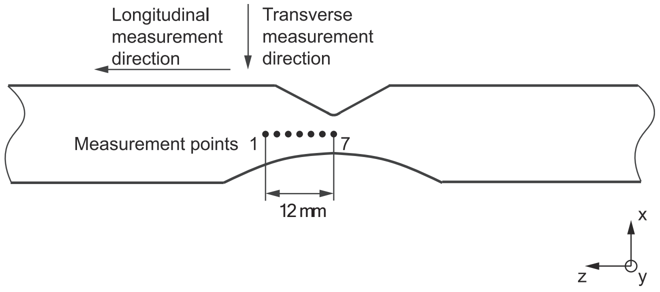

Fig. 9. Residual measurement locations towards the notch bisector.

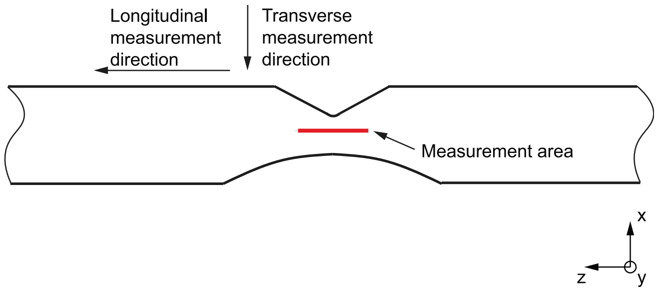

Fig. 10. Schematic illustration of the measurement area with the line focus for each spot.

$$\sigma(z_1) = \sigma_m(z_1) + \left(-4\sigma_m(H)\left(\frac{\Delta z_1}{H}\right)\right), \tag{1}$$

in which $\sigma(z_1)$ and $\sigma_m(z_1)$ are the actual and measured residual stresses of the sample with thickness z_1 after electropolishing, respectively, $\sigma_m(H)$ is the residual stress of the sample with thickness H. H is the original sheet thickness before electropolishing, z_1 is the thickness of the sample after electropolishing, and Δz_1 is the change in the thickness after electropolishing.

Fig. 11 presents the distribution of the surface residual stresses in the specimens. As can be seen the WAAM-specimen shows the highest residual stresses followed by PBF-LB/M specimen. The wrought sample has compressive on-surface residual stresses. It should be noted each measurement spot showed in this figure represent the weighted average of the residual stress in a 16 × 4.2 mm^2 area. Since the 16 mm line moves just 1 mm from the bisector at each measurement, the difference between different measurements is small. Horizontal error bars show the width covered by each measurement.

Fig. 12 illustrates the residual stress changes in the depth of the specimens. In this figure, the residual stresses of the WAAM sample first increase and then in deeper depths decrease to compressive residual

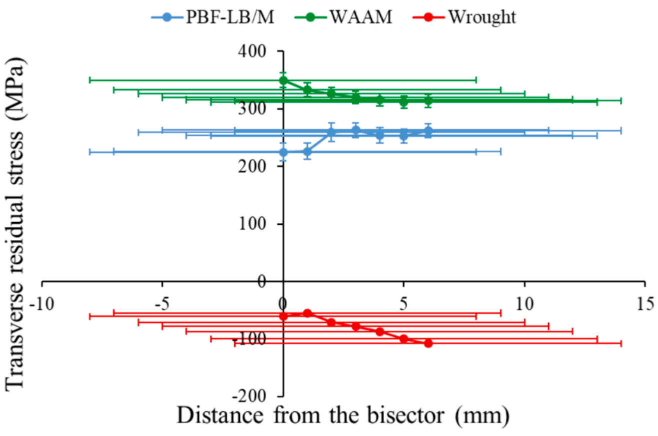

Fig. 11. On-surface residual stress distribution in V-notched 316L specimen.

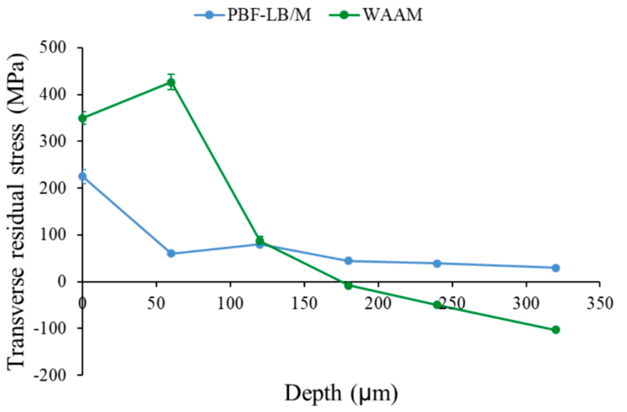

Fig. 12. In-depth residual stress distribution in V-notched 316L specimen.

stresses; however, PBF-LB/M sample shows a sudden drop in the residual stress values and in deeper depths the reduction is slighter. It is worth noting since the area covered and the penetration depth of the x-ray beam change by tilting the sample, the above residual stress values are the weighted average of the residual stresses of the specimen in the reflected volume.

There are still tensile residual stresses in the PBF-LB/M specimen despite the heat treatment; however, additional measurements before the heat treatment show that the heat treatment does in fact relieve residual stresses. This result agrees with observations by Sanchez-Poncela et al. [47], who showed that heat treatment temperatures below 800 °C reduce residual stresses in 316L PBF-LB/M parts while barely affecting the microstructure.

The results prove that there are differences in residual stress levels between the two AM materials. In general, higher tensile residual stresses were measured in the WAAM material and in particular at the surface compared to the PBF-LB/M material. This is not surprising as the heat input is higher in the WAAM process, which leads to higher temperature gradients. In addition, the PBF-LB/M specimens were heat treated, which partially relaxed residual stresses. It is assumed that this will lead to lower fatigue strength of the WAAM compared to the PBF-LB/M specimens. The near-surface compressive residual stresses at the wrought specimen can be explained by the plastic deformation of the surface due to the rolling process. Similar results regarding the residual stress state of wrought and PBF-LB/M 316L were reported in previous studies [25,45].

5. Experimental investigation of fatigue crack initiation and propagation behavior

5.1. Experimental set-up

Fatigue tests were carried out under force-controlled tensile loading with a stress ratio $R = \sigma_{\min}/\sigma_{\max} = 0$ at a test frequency of 8 Hz. Tests exceeding 2 million cycles were terminated and classified as run-outs (marked by arrows in Fig. 13). The fatigue test data is fitted to Basquin's equation by linear regression with

$$N = 10^6 \left(\frac{\Delta\sigma_n}{\Delta\sigma_R}\right)^{-k}, \tag{2}$$

where N is the endured number of cycles on the nominal stress range level $\Delta\sigma_n$, $\Delta\sigma_R$ is the reference fatigue strength at 10^6 cycles, and k the free inverse slope. Specimens that failed between 10^6 and 2×10^6 cycles were not included in the S-N curve assessment as 10^6 cycles is considered to be the approximate knee point of the S-N curves for specimens with such stress concentration factors. This assumption is based on an extensive investigation of artificially notched specimens presented in Braun et al. [48].

5.2. Fatigue test results

Besides the nominal stress results of each series, the results for the mean $\Delta\sigma_{R,50\%}$ and mean minus two standard deviations of the fatigue strength $\Delta\sigma_{R,97.7\%}$ (survival probability of $P_s = 97.7\%$) at 10^6 cycles, the scatter range T_σ between 2.3 % and 97.7 % survival probability (shaded area), as well as the inverse slope k (slope triangle) are presented in Fig. 13. In addition, Figs. 14 and 15 present comparisons for the three specimen geometries and for the different manufacturing processes, respectively.

Comparing the plain specimens, the highest fatigue strength is observed for the PBF-LB/M specimens, followed by the wrought material. The WAAM specimens showed the lowest fatigue strength. This is assumed to be related to the coarse grain microstructure and the high tensile residual stresses in the WAAM material compared to the other process routes. The higher fatigue strength of the plain PBF-LB/M specimens compared to the wrought counterparts, is most probably related to differences in the microstructure that affects static and cyclic material properties. The PBF-LB/M poses significantly higher yield and ultimate tensile strength compared to the wrought material, see [35,43]. In plain specimens with smooth surfaces, higher static material strength typically leads to higher fatigue strength.

The results for the WAAM and wrought material specimens show the expected fatigue behavior with a decrease of fatigue strength with increasing notch acuity. In contrast, the PBF-LB/M specimens show a similar fatigue strength for plain and V-notched specimens as the wrought material but a different behavior for the U-notched specimens, see Fig. 15. The S-N curve of the PBF-LB/M U-notched specimens, shown in Figs. 14(b) and 15(a), has a significantly steeper slope than those of the WAAM and wrought material specimens. In fact, the comparatively steep slope of the U-notched specimens results in nearly identical fatigue strengths for the U- and V-notched specimens at 1 million cycles. The corresponding fatigue strengths for 50 % and 97.7 % survival probability are only about 10 MPa apart. In principle, a higher fatigue strength would have been expected for both PBF-LB/M U-notched specimens compared to the V-notched specimens due to the lower stress concentration factor for the U-notched specimens. This is the case for the other two materials. The reasons for this behavior will subsequently be investigated in more detail based on the fatigue crack initiation and propagation behavior.

5.3. Assessment of fatigue crack initiation behavior

In order to be able to follow the crack initiation and propagation process during the tests, the specimens were equipped with crack strain gauges (type FAC-5 by Tokyo Measuring Instruments Laboratory Co., Ltd., see Fig. 16). These strain gauges are placed on both sides of the specimens and are located as close as possible to the root of the notch (spacing about 0.1 mm). The crack initiation criterion is defined as the tearing of the first strand. This typically corresponds to a full-thickness crack. As the crack grows, one strand after another breaks, resulting in a change in the measured voltage. In practice, this results in a staircase function, see Fig. 17, which can be used to determine the crack propagation rate as a function of the number of cycles.

Using the crack strain gauge, it is also possible to determine crack initiation. In this case, a crack length of 0.1 mm at the specimen surface was used as the crack initiation criterion. The results of a comparison of the fatigue crack initiation to fracture ratio R_c for the U- and V-notched specimens are shown in Fig. 18. In addition, Table 5 and 6 summarize the test results of all tested specimens.

The ratio of the number of cycles to crack initiation to the number of cycles to failure reflects the behavior of the S-N curves; however, scatter

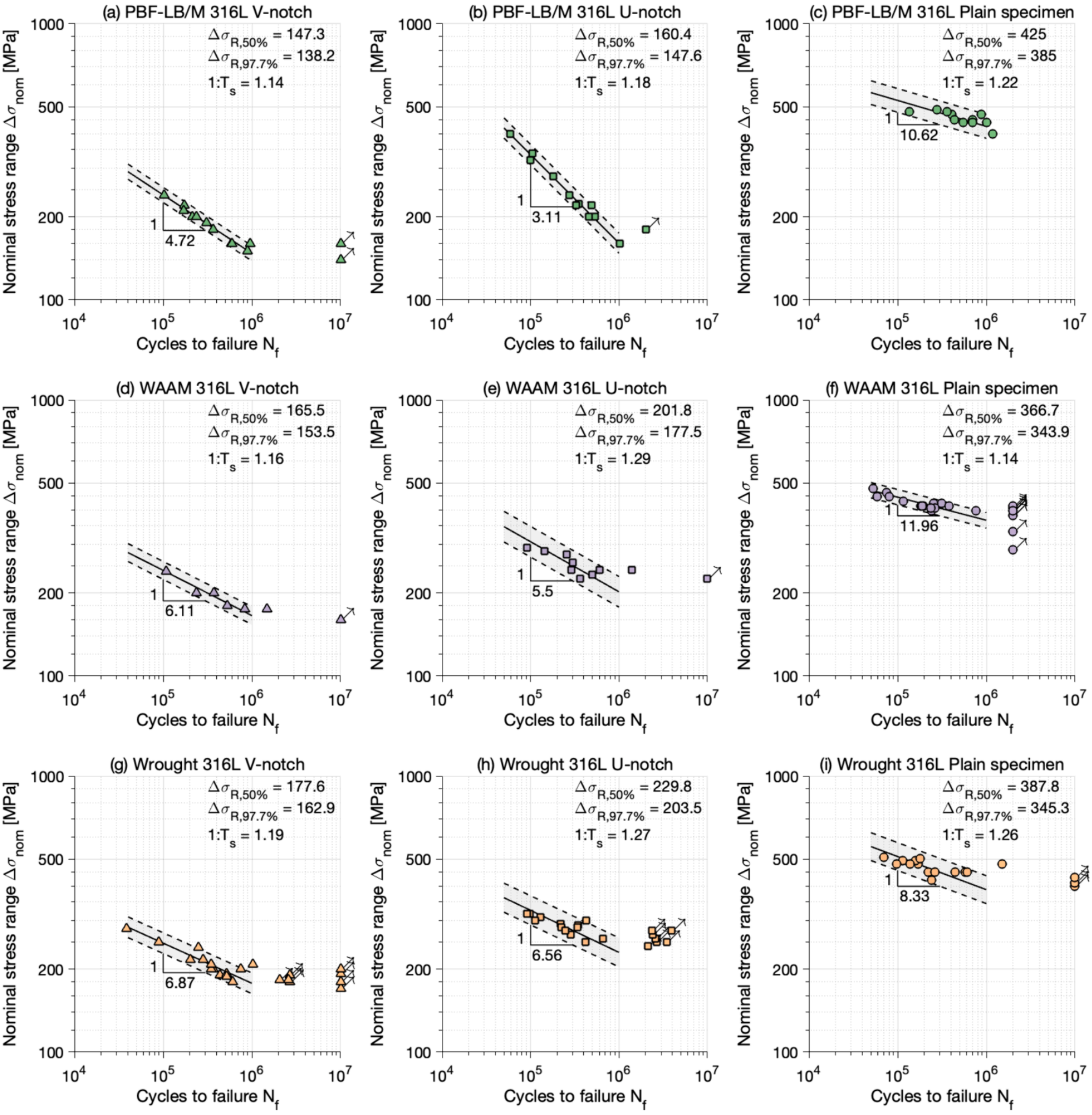

Fig. 13. Determined S-N curves for the three different processes at a nominal stress ratio of..$R = 0$

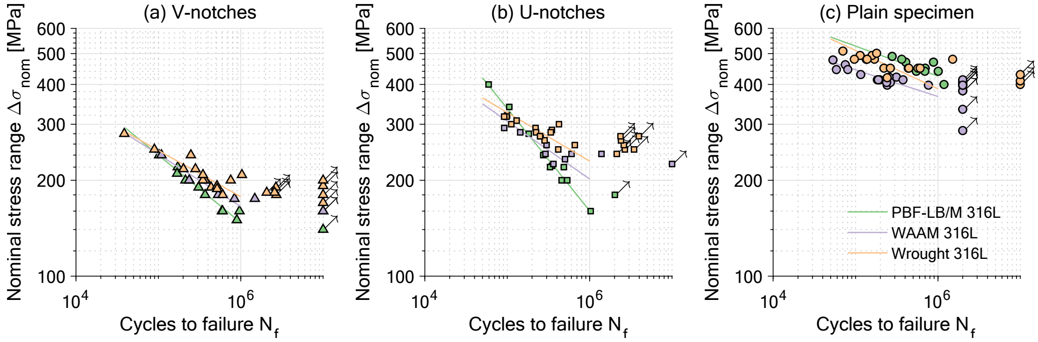

Fig. 14. Combined comparison of S-N curves for the three different specimen geometries.

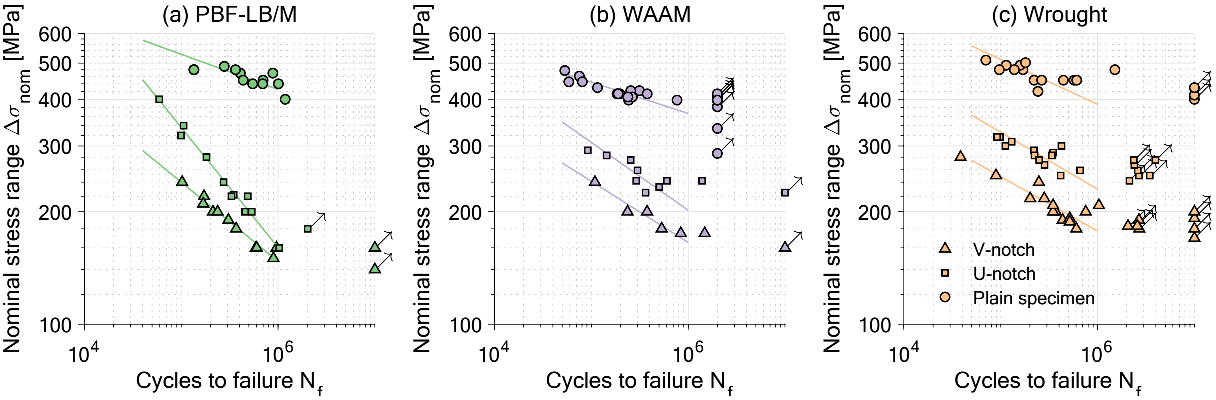

Fig. 15. Combined comparison of S-N curves for the three different processes.

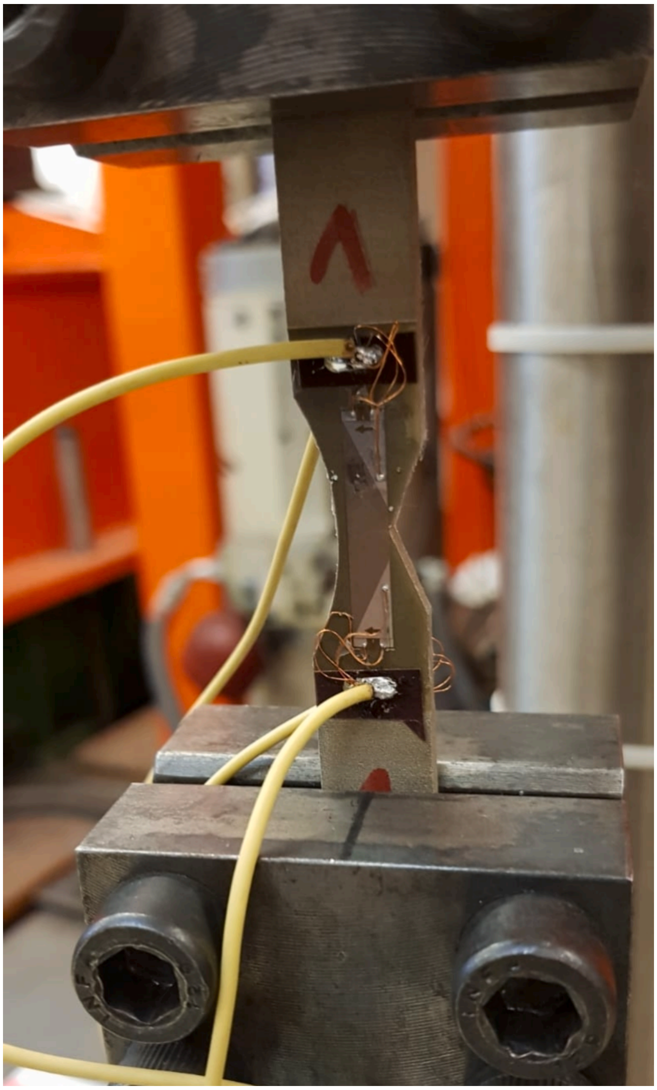

Fig. 16. Crack strain gauge on a V-notched PBF-LB/M specimen.

of the ratios is particularly high for the V-type specimens. In general, the V-type specimens with sharper notches experience an earlier crack initiation than the milder notched U-type specimens. Comparing the ratio at a nominal stress range of 200 MPa, a longer crack initiation life of the U-notched specimens is observed for the U-type specimens compared to the V-type specimens. This is the case for all test series expect for the U-notched PBF-LB/M specimens. For these specimens, an increase of the fatigue crack initiation to fracture ratio R_c is observed for increasing nominal stress ranges. This behavior is mainly related to differences in crack propagation behavior. This may be related to the defects near the plane with the smallest cross-sectional area found in the CT scans (Fig. 4(a)). This suggests that these defects led to an earlier fatigue crack initiation and acceleration of crack growth due to coalescence of fatigue crack and defects. In contrast, at high load levels the fatigue crack propagation phase is shorter, as final fracture occurs at shorter crack lengths. In general, the fatigue crack initiated the latest in the wrought material. This agrees well with the common knowledge that fine-grained microstructures yield favorable fatigue crack initiation behavior, see, e.g., Chen [11]. Compared to the AM materials, the hot-rolled and annealed steel specimens show a fine microstructure with equiaxed grains.

5.4. Assessment of fatigue crack propagation behavior

To compare the fatigue crack growth behavior, the number of cycles of fatigue crack propagation N_{fcg} (cycles to failure minus cycles to fatigue crack initiation) are shown in Fig. 19. Based on the S-N curves, it can be seen that both the fatigue crack initiation and the propagation behavior are different for all three materials. For the V-notched specimens, the difference is less pronounced than for the U-notched specimens. In particular the U-notched specimens fabricated by PBF-LB/M show an unexpected behavior. This can also be seen from a comparison of the curves for V- and U-notched specimens. The curves for the WAAM and wrought material specimens have similar slopes for both notch geometries, as the fatigue crack growth behavior is not influenced much by the notch shape once a technical crack has been initiated.

In the case of the U-notched specimens fabricated by PBF-LB/M, a much steeper slope is observed— indicating an accelerated fatigue crack growth, see Table 4. In addition, the standard deviation of the slope exponent for both PBF-LB/M test series is lower than for the other two materials. This indicates that there is some systematic influence of the fatigue crack growth behavior or all specimens. Potentially, the line-type defect clusters of pores, which are aligned with the scanning pattern of the PBF-LB/M process caused an acceleration of fatigue crack growth. As all specimens within the two PBF-LB/M test series show a similar fatigue crack propagation behavior, it is likely that the same type of imperfection is responsible for this effect.

Interestingly, the slope of the V-notched PBF-LB/M specimen test series is not as steep as for the U-notched specimens of the same material. This may be attributed to a less severe impact of imperfections for the V-notched PBF-LB/M specimen or simply the higher impact of the macro geometric notch. This is supported by the large difference in stress concentration factors. The stress concentration factor of the V-notched specimens is about three times larger than for the U-notched

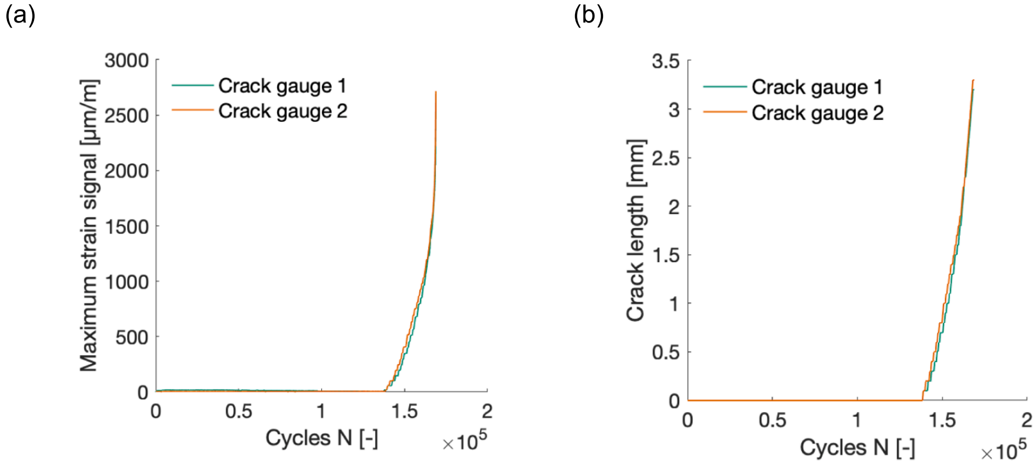

Fig. 17. Measurement of the signal of a crack strain gauge (a) on a V-notched specimen manufactured by PBF-LB/M process and derived crack growth (b).

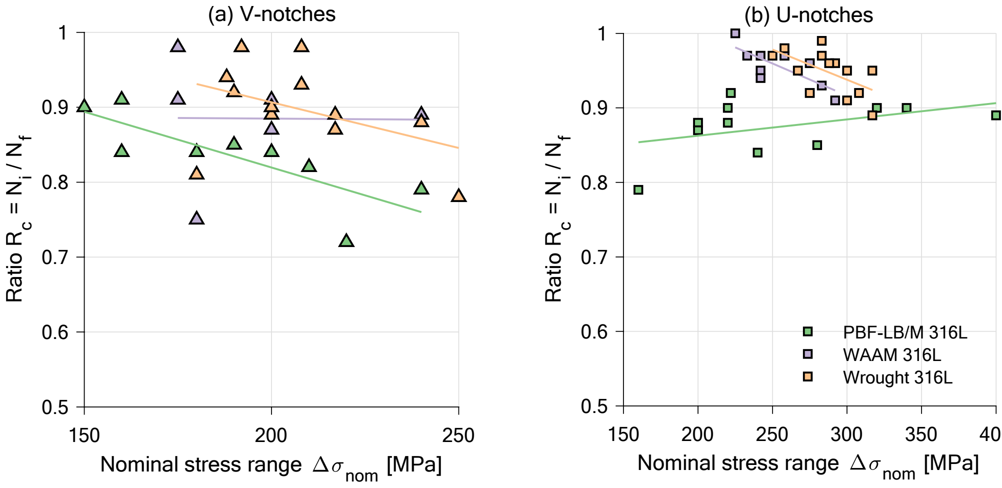

Fig. 18. Determined ratio between number of cycles to crack initiation and number of cycles to fracture for (a) V-notch and (b) U-notch specimens; including trend lines.

specimens ($K_t = 5.75$ and $K_t = 1.87$, respectively).

In addition to the differences in slope exponents k, there are also differences in the reference fatigue strength at 10^6 cycles $\Delta\sigma_R$ of the curves, see Table 4. The wrought material generally shows the best fatigue crack propagation behavior (highest fatigue strength between 10^5 to 10^6 cycles). This is clearly related to the tensile residual stresses in both AM materials. The microstructure of the materials also influences the fatigue crack propagation behavior. In theory, higher fatigue crack propagation rates are expected in the finer grained material; yet, the wrought material with the finest microstructure shows the lowest propagation rates, i.e., best fatigue crack growth resistance. This indicates that the effect of residual stresses and imperfections is stronger for the notched test specimens than the microstructural effects. Finally, a better fatigue crack propagation behavior of PBF-LB/M specimens compared to the WAAM counterparts would have been expected due to the higher tensile residual stress in the WAAM material; however, the opposite is the case. This is thought to be related to the line-type defect clusters of pores and other imperfections.

6. Fracture surface investigations

The fracture surfaces of the V- and U-notched samples were analyzed using scanning electron microscopy (SEM). The scans reveal heterogeneous surface topographies characterized by regions of varying roughness. Macroscopically, the fracture surfaces displayed a mixture of smooth and rough areas, indicative the different stages of crack propagation. At higher magnifications, crack initiation sites are clearly identifiable. The number of crack initiation sites vary with material and specimen type.

The V-notched specimens with high notch acuity show several sites for all three materials, while the U-notched specimens show only one or a few initiation sites. These initiation points were predominantly located near imperfections typical for the AM process, such as porosities close to the machined surface (see the U-notch PBF-LB/M specimen in Fig. 20 (b)). On some specimens, ratched marks indicate multiple fatigue crack initiation sites in different planes in z-direction that later coalesced. This can be seen from the lines approximately parallel to the fatigue crack growth direction, e.g., in Fig. 20(a) I or Fig. 20(c) I). In both PBF-LB/M specimens, line-type defect clusters of pores are found in the fracture surfaces, acting as stress raisers that accelerate crack propagation. The presence of these defects confirms—that were also observed by CT scans—confirm the assumption that these defects are dominating the fatigue behavior of the PBF-LB/M specimens. In addition, they underscore the need for optimized processing parameters to minimize imperfection and to improve the fatigue strength of PBF-LB/M components. In Fig. 20(c) II, an imperfection is magnified in the fracture surface of a V-notched WAAM specimen. This imperfection, however, didn’t cause a fatigue crack to initiate. The stress concentration at the

Table 5
Test results of the V-notched specimens.

Material	Stress range Δσ [MPa]	Number of cycles to failure N_f	Number of cycles to crack initiation N_i	Test result	Ratio $R_c = N_i/N_f$
Wrought	280	38,505	–*	fracture	–*
Wrought	250	89,454	69,637	fracture	0.78
Wrought	217	201,484	178,945	fracture	0.89
Wrought	240	247,818	218,995	fracture	0.88
Wrought	217	281,733	244,663	fracture	0.87
Wrought	200	347,141	–*	fracture	–*
Wrought	208	347,221	321,693	fracture	0.93
Wrought	200	369,481	329,994	fracture	0.89
Wrought	190	436,200	400,549	fracture	0.92
Wrought	192	515,532	502,846	fracture	0.98
Wrought	188	516,299	486,962	fracture	0.94
Wrought	180	603,574	491,417	fracture	0.81
Wrought	200	754,651	680,828	fracture	0.90
Wrought	208	1,031,849	1,015,420	fracture	0.98
Wrought	183	2,063,734	–	run-out	–
Wrought	183	2,571,273	–	run-out	–
Wrought	190	2,673,288	–	run-out	–
Wrought	180	2,700,129	–	run-out	–
Wrought	170	10,000,000	–	run-out	–
Wrought	192	10,000,000	–	run-out	–
Wrought	200	10,000,000	–	run-out	–
Wrought	180	10,248,220	–	run-out	–
WAAM	240	108,791	96,311	fracture	0.89
WAAM	200	236,283	204,844	fracture	0.87
WAAM	200	376,208	340,571	fracture	0.91
WAAM	180	532,000	399,510	fracture	0.75
WAAM	175	838,287	764,633	fracture	0.91
WAAM	175	1,481,735	1,447,099	fracture	0.98
WAAM	160	10,000,000	–	run-out	–
PBF-LB/M	240	102,123	80,826	fracture	0.79
PBF-LB/M	210	168,882	138,807	fracture	0.82
PBF-LB/M	220	171,908	124,098	fracture	0.72
PBF-LB/M	200	212,952	–*	fracture	–*
PBF-LB/M	200	237,942	200,547	fracture	0.84
PBF-LB/M	190	307,169	262,351	fracture	0.85
PBF-LB/M	180	369,025	308,834	fracture	0.84
PBF-LB/M	160	590,069	498,593	fracture	0.84
PBF-LB/M	160	601,927	–*	fracture	–*
PBF-LB/M	150	895,405	801,607	fracture	0.90
PBF-LB/M	160	964,907	880,723	fracture	0.91
PBF-LB/M	80	10,000,000	–	run-out	–
PBF-LB/M	140	10,000,000	–	run-out	–

* Due to failed crack gauges.

Table 6
Test results of the U-notched specimens.

Material	Stress range Δσ [MPa]	Number of cycles to failure N_f	Number of cycles to crack initiation N_i	Test result	Ratio $R_c = N_i/N_f$
Wrought	317	91,731	87,056	fracture	0.95
Wrought	317	98,171	87,473	fracture	0.89
Wrought	300	111,717	101,874	fracture	0.91
Wrought	308	129,814	119,618	fracture	0.92
Wrought	292	220,373	211,110	fracture	0.96
Wrought	283	223,607	217,306	fracture	0.97
Wrought	275	249,456	229,812	fracture	0.92
Wrought	267	283,473	270,633	fracture	0.95
Wrought	283	337,118	332,579	fracture	0.99
Wrought	288	347,909	334,081	fracture	0.96
Wrought	250	415,552	404,374	fracture	0.97
Wrought	300	424,117	403,889	fracture	0.95
Wrought	258	660,562	650,553	fracture	0.98
Wrought	242	2,134,445	–	run-out	–
Wrought	275	2,366,590	–	run-out	–
Wrought	267	2,400,000	–	run-out	–
Wrought	258	2,598,329	–	run-out	–
Wrought	250	2,676,338	–	run-out	–
Wrought	250	3,456,187	–	run-out	–
Wrought	275	3,955,089	–	run-out	–
WAAM	292	91,773	83,497	fracture	0.91
WAAM	283	143,594	132,935	fracture	0.93
WAAM	275	254,583	243,804	fracture	0.96
WAAM	242	290,659	276,176	fracture	0.95
WAAM	258	299,796	291,123	fracture	0.97
WAAM	225	363,082	363,082	fracture	1.00
WAAM	233	501,442	485,726	fracture	0.97
WAAM	242	602,295	564,037	fracture	0.94
WAAM	242	1,391,709	1,354,104	fracture	0.97
WAAM	225	10,000,000	–	run-out	–
PBF-LB/M	400	59,360	52,536	fracture	0.89
PBF-LB/M	320	99,544	89,274	fracture	0.90
PBF-LB/M	340	105,677	95,311	fracture	0.90
PBF-LB/M	280	182,212	154,854	fracture	0.85
PBF-LB/M	240	273,381	229,882	fracture	0.84
PBF-LB/M	220	330,215	291,156	fracture	0.88
PBF-LB/M	222	348,233	320,234	fracture	0.92
PBF-LB/M	200	457,010	399,432	fracture	0.87
PBF-LB/M	220	485,912	437,470	fracture	0.90
PBF-LB/M	200	534,284	468,419	fracture	0.88
PBF-LB/M	160	1,027,860	814,412	fracture	0.79
PBF-LB/M	180	2,023,072	–	run-out	–

notch tip must have been larger.

Finally, the SEM analysis of the PBF-LB/M and wrought material specimens reveal regions in the final fracture area with voids, indicating a ductile fracture mechanism. In contrast, no voids are observed in the WAAM specimens don’t show voids; however, the significant necking also indicates a ductile failure by plastic collapse.

7. Discussion

Based on the comparison, there is strong evidence that the difference in fatigue behavior is driven by a variety of influencing factors. For plain specimens without notches and with smooth surfaces, the highest fatigue strength is observed the PBF-LB/M specimens, followed by the wrought and WAAM specimens. The difference in fatigue strength for the plain specimens is likely related to differences in microstructure, which can be confirmed by the EBSD measurements, see Figs. 6 and 7. In general, the microstructure with fine grains and more HAGBs performs better in fatigue, see [11,13], and the microstructure with large strong textured columnar grains shows weak and undesired anisotropic fatigue properties [44]. For wrought 316L stainless steel produced by hot-rolling and annealing, the fine equiaxed grains and the high proportion of HAGBs help to hinder the initiation of the crack during fatigue testing, resulting in high fatigue strength. For 316L stainless steel fabricated by WAAM with large strong textured columnar grains, the initiation of crack is easier due to the unfavorable microstructure, and the crack propagation is faster due to high tensile residual stresses. Therefore, the WAAM 316L stainless steel showed the lowest fatigue

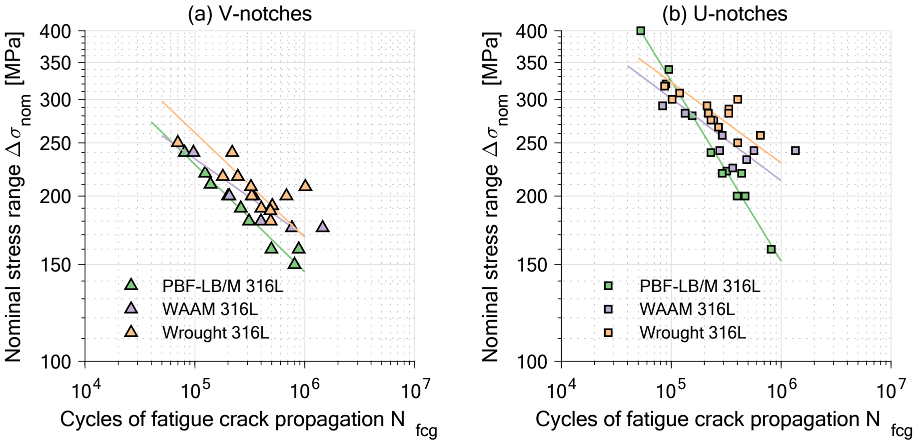

Fig. 19. Number of cycles of fatigue crack propagation N_{fcg} for (a) V-notch and (b) U-notch specimens.

Table 4
Parameters of the fatigue crack propagation S-N curves.

Specimen type	Material	Slope exponent k	Standard deviation of the slope exponent	Reference fatigue strength at 10^6 cycles $\Delta\sigma_R$	Scatter range T_σ
V-notch	PBF-LB/M	5.12	0.37	145.5	1.14
	WAAM	7.12	1.64	169.1	1.28
	Wrought	5.25	1.51	168.1	1.45
U-notch	PBF-LB/M	3.05	0.15	152.1	1.19
	WAAM	6.68	2.21	213.3	1.41
	Wrought	6.8	1.6	229.8	1.27

performance of the plain fatigue test specimens. The PBF-LB/M specimens possess the highest fatigue strength in plain state. The reason is likely related to the high yield and ultimate tensile strength of the PBF-LB/M specimens compared to the wrought material, see [35,43]. Higher static strength typically leads to a better fatigue performance.

Besides microstructural influences, the effects of process-related residual stresses are apparent, see Figs. 11 and 12. High tensile residual stresses were determined towards and in the middle of the notch bisector of a V-notched PBF-LB/M specimen, which decrease in depth direction. Even higher tensile residual stresses were found in the WAAM U- and V-notched specimens and particularly at the surface of the two measured specimens. This is likely related to the higher heat input during the WAAM process; however, the PBF-LB/M specimens were also heat treated, which partially relaxed residual stresses. In contrast, the hot-rolled and annealed specimens showed minor compressive residual stresses. Based on the high tensile residual stresses at the surface in both the PBF-LB/M and the WAAM specimens, it also makes sense that the fatigue crack initiation happened earlier for these two materials. The effect of the residual stresses on fatigue crack propagation can, however, not be fully determined based on the available experimental data. During early fatigue crack propagation, the tensile residual stresses in both AM materials will increase the crack propagation rate. At about 100 μm in depth, the residual stresses are already much lower but still higher in the WAAM material. The effect will thus be less pronounced. Neutron diffraction measurements would be required to investigate this in more depth by determining the residual stresses gradients through the full thickness.

Comparing the S-N curves of notched specimens, a large difference is found for V-notched specimens with moderate opening angle and U-notched specimens with 180° opening angle. For the V-notched specimens, the difference in fatigue life is found to be partially related to an earlier fatigue crack initiation in PBF-LB/M specimens compared to wrought and WAAM specimens as well as a shorter fatigue crack propagation life. For the U-notched specimens, a high fatigue strength is observed at low number of cycles to failure, which is followed by a steep S-N curve and significantly lower fatigue strength at lower stress levels. This is also confirmed by an earlier fatigue crack initiation compared to the two other materials.

The fatigue crack growth in the notched PBF-LB/M specimen is accelerated by line-type defects, as observed in the micrographs, CT scans, and fracture surface investigations by SEM, see Figs. 4 and 5. The pores are aligned with the scan pattern of the PBF-LB/M process, involving a rotation of the scanning pattern by 67°. While each individual defect is relatively small and, on average, separated by more than twice its diameter, their arrangement within the same plane perpendicular to the loading direction could potentially accelerate fatigue crack propagation. These pores could be caused by changes in heat input at the start-stop position, as the processing parameter for these locations might be outside of the optimal power-velocity processing parameter space.

Such defects have also been observed in the plain test specimens, see Braun et al. [35]; however, these specimens are characterized by a long crack initiation and short fatigue crack propagation phase. Therefore, these specimens will not be influenced much by such defects. It is possible that this effect is more pronounced in the U-type PBF-LB/M specimen, as larger defects were observed in the exemplary CT scan of this specimen type compared to the V-type specimen. Thus, the presence of even minor defects can greatly diminish the fatigue performance, particularly if these defects are located in unfavorable positions or when multiple small defects are clustered together; however, the impact of these defects is largely influenced by the applied load level and the relation between the crack initiation and propagation phases.

These pores were found at start-stop positions of the scanning pattern of the PBF-LB/M process. Each defect is individually rather small; however, due to the alignment with the same plane perpendicular to the loading direction the fatigue crack propagation is likely accelerated. Such defects have also been observed in the plain specimens; but the fatigue life of the plain specimens is predominantly determined by fatigue crack initiation. Thus, the fatigue strength of the plain PBF-LB/M specimens is not greatly affected.

Unfortunately, the U-type specimens are not as well suited for measuring fatigue crack growth rates due to the required high loads if tests are performed under constant amplitude loading. At high stress levels, failure of the specimens occurs shortly after crack initiation, which is associated with large plastic zones ahead of the crack tip. To investigate the fatigue crack initiation behavior in mildly notched specimens—such as the U-notched specimens in this study—in more detail, future tests could interrupt the test after fatigue crack initiation

(a) Wrought material

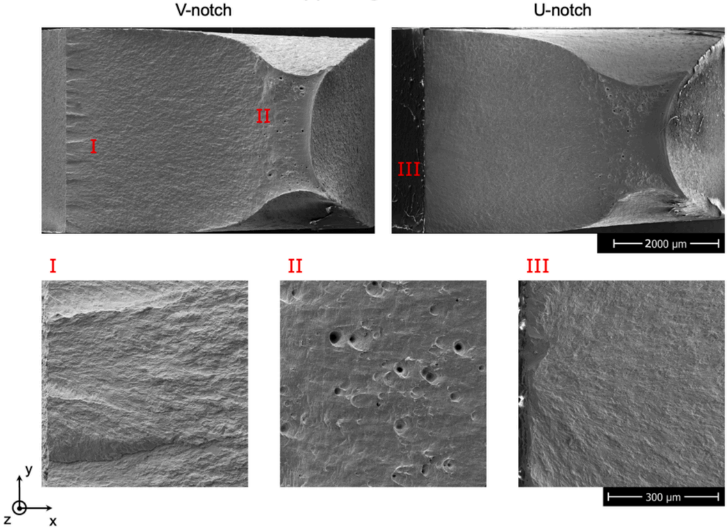

(b) PBF-LB/M

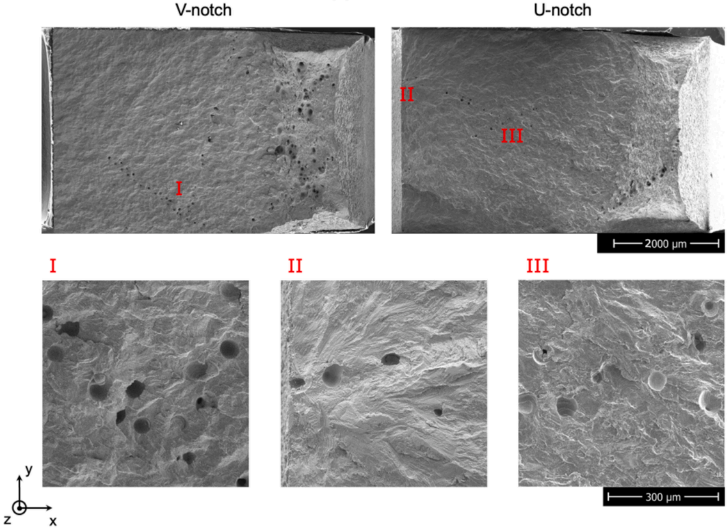

(c) WAAM

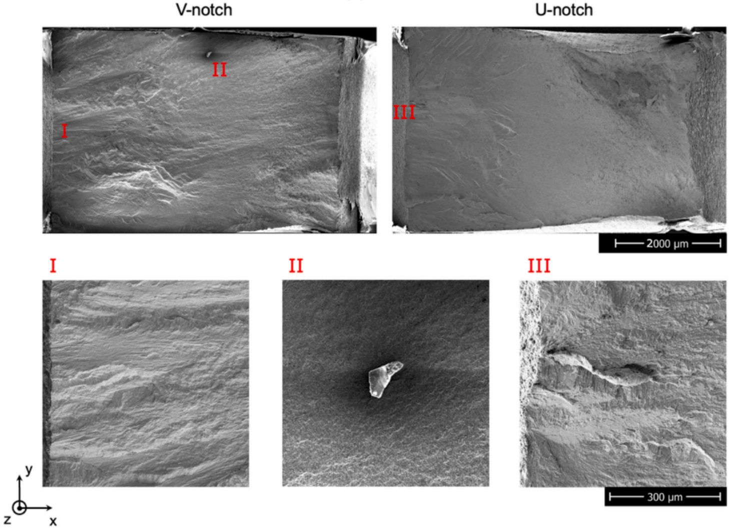

Fig. 20. Scanning electron fracture surface investigations of the two notched specimen types and three different materials with highlighted regions.

and continue with K-decreasing tests, such as those recommended by ASTM E647 [49].

8. Summary and conclusions

This study compared the fatigue strength as well as fatigue crack initiation and propagation behavior of machined 316L additively manufactured components—fabricated using PBF-LB/M and WAAM processes—to components made from conventional hot-rolled and annealed sheet material, as there are hardly any studies on the fatigue behavior of notched AM components with machined surfaces. In addition, the study delved into the influence of notches on the fatigue strength to assess the importance of geometric features in actual applications where stress concentrations may arise. Experimental investigations were conducted on two notch configurations and plain specimens without notches. The study used various experimental test methods to analyze the inherent material differences between additively manufactured parts and their conventionally produced counterparts. The fatigue strength of additive manufactured materials is significantly characterized by influencing factors such as microstructure, defects, residual stress states, and macro-geometric notches. For plain specimens without notches and with smooth surfaces, the highest fatigue strength is observed for PBF-LB/M specimens, followed by wrought, and WAAM specimens. In notched state, higher fatigue strength is observed for the wrought material. Based on the results obtained, the following conclusions are drawn:

- The fatigue behavior of plain specimens is strongly influenced by microstructural differences. Fine equiaxed grains and a high proportion of high-angle grain boundaries contribute to superior fatigue strength, as observed in wrought 316L stainless steel. Conversely, specimens with large, strong textured columnar grains, such as those fabricated by WAAM, exhibit weaker fatigue properties due to easier crack initiation and faster crack propagation. For wrought 316L stainless steel produced by hot-rolling and annealing, the fine equiaxed grains and the high proportion of high-angle grain boundaries help to hinder fatigue crack initiation. The high fatigue strength of the plain PBF-LB/M specimens is attributed to the high static strength, which stems from multi-scale microstructural features such as cellular dislocation substructures and a bimodal grain size distribution with large columnar grains and fine equiaxed grains.
- Residual stresses resulting from manufacturing processes significantly affect fatigue performance. High tensile residual stresses, particularly evident at the surface of WAAM specimens, contribute to lower fatigue strength. This is related to the high heat input during the WAAM process leads to a detrimental residual stress state. Conversely, hot-rolled and annealed specimens exhibit minor compressive residual stresses, which enhance fatigue resistance.
- Notched specimens display notable differences in fatigue behavior compared to plain specimens. V-notched specimens exhibit earlier fatigue crack initiation and shorter fatigue crack propagation life, particularly in PBF-LB/M specimens. This is found to be partially related to differences in fatigue crack initiation and shorter fatigue crack propagation life for PBF-LB/M specimens. Both are likely related to line-type defect clusters of pores that were observed by CT scans and fracture surface investigations by SEM.
- Fatigue crack growth in notched PBF-LB/M specimens, is accelerated by line-type defects, i.e., pores aligned with the scanning pattern of the additive manufacturing process. These defects, caused by sub-optimal processing parameters, can significantly diminish fatigue performance, particularly when clustered together or located unfavorably; however, the impact of these defects depends on factors such as the applied load level and the relationship between crack initiation and propagation phases. The fatigue strength of the plain PBF-LB/M specimens is not greatly affected, as it is predominantly defined by fatigue crack initiation.

Overall, the study shows that even small defects can lead to significant reductions in fatigue performance if they are located in unfavorable positions or if several small defects are found close to each other; however, the severity of such defects is related to the applied external load and the ratio of cycles to fatigue crack initiation and propagation.

9. Outlook

This study has provided significant insights into the fatigue crack initiation and propagation behavior in plain and notched 316L stainless steel specimens taken from PBF-LB/M, WAAM, and wrought material.

Logical next steps would be the application of advanced fatigue assessment methods to enabled a comprehensive evaluation of the fatigue performance but also facilitated the determination of critical material properties, such as notch sensitivity factors, see [50,51]. These findings will contribute to a deeper understanding of the fatigue characteristics of additively manufactured components in contrast to traditionally manufactured components.

Future research will focus on expanding the dataset through additional tests, which will enhance the robustness of the analysis. With more extensive test data, the application of statistical models like the Stromeyer equation [52] or the maximum likelihood approach [53,54] can be employed to describe the kneepoints of the S-N curves more accurately. These models will enable a more precise prediction of the fatigue life and a better understanding of the transition between different fatigue regimes.

Moreover, continued investigation into the microstructural features influencing fatigue behavior in PBF-LB/M and WAAM specimens will be crucial. This will involve correlating the fatigue performance with the specific microstructural attributes inherent to these manufacturing processes. The ultimate goal is to develop predictive models that can account for the unique characteristics of each manufacturing method, thus providing engineers with reliable tools for fatigue life prediction and structural integrity assessment.

CRediT authorship contribution statement

Moritz Braun: Writing – original draft, Visualization, Validation, Resources, Project administration, Methodology, Investigation, Funding acquisition, Formal analysis, Data curation, Conceptualization. **Ting Chen:** Writing – original draft, Visualization, Investigation, Formal analysis, Data curation. **Junjun Shen:** Investigation, Formal analysis, Conceptualization. **Henrik Fassmer:** Investigation, Formal analysis, Data curation. **Benjamin Klusemann:** Writing – review & editing, Supervision, Resources, Methodology, Funding acquisition. **Shahram Sheikhi:** Writing – review & editing, Funding acquisition, Conceptualization. **Sören Ehlers:** Writing – review & editing, Supervision, Resources, Funding acquisition. **Eckehard Müller:** Writing – original draft, Investigation, Conceptualization. **Ardeshir Sarmast:** Writing – original draft, Visualization, Investigation, Formal analysis, Data curation. **Jan Schubnell:** Writing – review & editing, Validation, Supervision, Resources.

Declaration of competing interest

The authors declare that they have no known competing financial interests or personal relationships that could have appeared to influence the work reported in this paper.

Data availability

Data will be made available on request.

Acknowledgements

The authors would like to sincerely thank the Yxlon company for their support by performing the CT scans. In addition, the preparation of the test specimens with crack gauges by Franziska Rolof and performing the scanning electron microscopy measurements by Xiru Wang is acknowledged. The work was performed within the research project LAYER – "Lebensdauersteigerung von additive gefertigten (DED) Bauteilen mittels hybrider Fertigungsverfahren" funded by the German Federal Ministry for Economic Affairs and Climate Action (project number 03SX592D). The group of B.K. acknowledge funding by the Deutsche Forschungsgemeinschaft (DFG, German Research Foundation) - project number 459713992.

References

[1] U. Zerbst, G. Bruno, J.Y. Buffiere, T. Wegener, T. Niendorf, T. Wu, X. Zhang, N. Kashaev, G. Meneghetti, N. Hrabe, M. Madia, T. Werner, K. Hilgenberg, M. Koukolikova, R. Prochazka, J. Dzugan, B. Moller, S. Beretta, A. Evans, R. Wagener, K. Schnabel, Damage tolerant design of additively manufactured metallic components subjected to cyclic loading: State of the art and challenges, Prog. Mater. Sci. 121 (2021), https://doi.org/10.1016/j.pmatsci.2021.100786.

[2] A. Yadollahi, N. Shamsaei, Additive manufacturing of fatigue resistant materials: Challenges and opportunities, Int. J. Fatigue 98 (2017) 14–31, https://doi.org/10.1016/j.ijfatigue.2017.01.001.

[3] N. Haghdadi, M. Laleh, M. Moyle, S. Primig, Additive manufacturing of steels: a review of achievements and challenges, J. Mater. Sci. 56 (2020) 64–107, https://doi.org/10.1007/s10853-020-05109-0.

[4] K. Solberg, Fatigue design for metallic components produced by additive manufacturing, Norwegian University of Science and Technology, 2021 [Doctoral Thesis].

[5] M. Kahlin, H. Ansell, J.J. Moverare, Fatigue behaviour of notched additive manufactured Ti6Al4V with as-built surfaces, Int. J. Fatigue 101 (2017) 51–60, https://doi.org/10.1016/j.ijfatigue.2017.04.009.

[6] C. Elangeswaran, A. Cutolo, G.K. Muralidharan, C. de Formanoir, F. Berto, K. Vanmeensel, B. Van Hooreweder, Effect of post-treatments on the fatigue behaviour of 316L stainless steel manufactured by laser powder bed fusion, Int. J. Fatigue 123 (2019) 31–39, https://doi.org/10.1016/j.ijfatigue.2019.01.013.

[7] D.A. Lesyk, S. Martinez, B.N. Mordyuk, V.V. Dzhemelinskyi, A. Lamikiz, G. I. Prokopenko, Post-processing of the Inconel 718 alloy parts fabricated by selective laser melting: Effects of mechanical surface treatments on surface topography, porosity, hardness and residual stress, Surf. Coat. Technol. 381 (2020), https://doi.org/10.1016/j.surfcoat.2019.125136.

[8] P. Sandmann, S. Keller, N. Kashaev, S. Ghouse, P.A. Hooper, B. Klusemann, C. M. Davies, Influence of laser shock peening on the residual stresses in additively manufactured 316L by Laser Powder Bed Fusion: A combined experimental–numerical study, Addit. Manuf. 60 (2022), https://doi.org/10.1016/j.addma.2022.103204.

[9] E. Maleki, S. Bagherifard, S.M.J. Razavi, M. Riccio, M. Bandini, A. du Plessis, F. Berto, M. Guagliano, Fatigue behaviour of notched laser powder bed fusion AlSi10Mg after thermal and mechanical surface post-processing, Mater. Sci. Eng. A 829 (2022), https://doi.org/10.1016/j.msea.2021.142145.

[10] E. Maleki, N. Shamsaei, A comprehensive study on the effects of surface post-processing on fatigue performance of additively manufactured AlSi10Mg: An augmented machine learning perspective on experimental observations, Addit. Manuf. 86 (2024) 104179, https://doi.org/10.1016/j.addma.2024.104179.

[11] K.S. Chan, Roles of microstructure in fatigue crack initiation, Int. J. Fatigue 32 (2010) 1428–1447, https://doi.org/10.1016/j.ijfatigue.2009.10.005.

[12] M.D. Sangid, The physics of fatigue crack initiation, Int. J. Fatigue 57 (2013) 58–72, https://doi.org/10.1016/j.ijfatigue.2012.10.009.

[13] Y. Estrin, A. Vinogradov, Fatigue behaviour of light alloys with ultrafine grain structure produced by severe plastic deformation: An overview, Int. J. Fatigue 32 (2010) 898–907, https://doi.org/10.1016/j.ijfatigue.2009.06.022.

[14] Y. Huang, T.G. Fleming, S.J. Clark, S. Marussi, K. Fezzaa, J. Thiyagalingam, C.L. A. Leung, P.D. Lee, Keyhole fluctuation and pore formation mechanisms during laser powder bed fusion additive manufacturing, Nat. Commun. 13 (2022) 1170, https://doi.org/10.1038/s41467-022-28694-x.

[15] R. Cunningham, C. Zhao, N. Parab, C. Kantzos, J. Pauza, K. Fezzaa, T. Sun, A. D. Rollett, Keyhole threshold and morphology in laser melting revealed by ultrahigh-speed x-ray imaging, Science 363 (2019) 849–852, https://doi.org/10.1126/science.aav4687.

[16] B. Tomar, S. Shiva, T. Nath, A review on wire arc additive manufacturing: Processing parameters, defects, quality improvement and recent advances, Mater. Today Commun. 31 (2022), https://doi.org/10.1016/j.mtcomm.2022.103739.

[17] N.A. Rosli, M.R. Alkahari, M.F.b. Abdollah, S. Maidin, F.R. Ramli, S.G. Herawan, Review on effect of heat input for wire arc additive manufacturing process, J. Mater. Res. Technol. 11 (2021) 2127–2145, https://doi.org/10.1016/j.jmrt.2021.02.002.

[18] A. Ermakova, S. Ganguly, N. Razavi, F. Berto, A. Mehmanparast, Experimental investigation of the fatigue crack growth behavior in wire arc additively manufactured ER100S-1 steel specimens, Fatigue Fract. Eng. M 45 (2021) 371–385, https://doi.org/10.1111/ffe.13598.

[19] M. Odnobokova, V. Torganchuk, M. Tikhonova, P. Dolzhenko, R. Kaibyshev, A. Belyakov, On the Strength of a 316L-Type Austenitic Stainless Steel Produced by Selective Laser Melting, Metals 13 (2023), https://doi.org/10.3390/met13081423.

[20] J. Suryawanshi, K.G. Prashanth, U. Ramamurty, Mechanical behavior of selective laser melted 316L stainless steel, Mater. Sci. Eng. A 696 (2017) 113–121, https://doi.org/10.1016/j.msea.2017.04.058.

[21] C. Wang, T.G. Liu, P. Zhu, Y.H. Lu, T. Shoji, Study on microstructure and tensile properties of 316L stainless steel fabricated by CMT wire and arc additive manufacturing, Mater. Sci. Eng. A 796 (2020), https://doi.org/10.1016/j.msea.2020.140006.

[22] R. Scharf-Wildenhain, A. Haelsig, J. Hensel, K. Wandtke, D. Schroepfer, A. Kromm, T. Kannengiesser, Influence of heat control on properties and residual stresses of additive-welded high-strength steel components, Metals 12 (2022), https://doi.org/10.3390/met12060951.

[23] R.D.K. Misra, S. Nayak, S.A. Mali, J.S. Shah, M.C. Somani, L.P. Karjalainen, Microstructure and deformation behavior of phase-reversion-induced nanograined/ultrafine-grained austenitic stainless steel, Metall. Mater. Trans. A 40 (2009) 2498–2509, https://doi.org/10.1007/s11661-009-9920-3.

[24] M. Odnobokova, Z. Yanushkevich, R. Kaibyshev, A. Belyakov, On the strength of a 316L-type stainless steel subjected to cold or warm rolling followed by annealing, Materials (Basel) 13 (2020), https://doi.org/10.3390/ma13092116.

[25] J. Schubnell, A. Sarmast, F. Altenhöner, S. Sheikhi, M. Braun, S. Ehlers, Residual stress analysis of butt welds made of additively and traditionally manufactured 316L stainless steel plates. Procedia Structural Integrity, in press (2022).

[26] D. Guo, K. Yan, M.D. Callaghan, D. Daisenberger, M. Chatterton, J. Chen, A. Wisbey, W. Mirihanage, Solidification microstructure and residual stress correlations in direct energy deposited type 316L stainless steel, Mater. Des. 207 (2021), https://doi.org/10.1016/j.matdes.2021.109782.

[27] P. Bian, J. Shi, Y. Liu, Y. Xie, Influence of laser power and scanning strategy on residual stress distribution in additively manufactured 316L steel, Opt. Laser Technol. 132 (2020), https://doi.org/10.1016/j.optlastec.2020.106477.

[28] A.S. Wu, D.W. Brown, M. Kumar, G.F. Gallegos, W.E. King, An Experimental Investigation into Additive Manufacturing-Induced Residual Stresses in 316L Stainless Steel, Metall. Mater. Trans. A 45 (2014) 6260–6270, https://doi.org/10.1007/s11661-014-2549-x.

[29] Y. Liu, Y. Yang, D. Wang, A study on the residual stress during selective laser melting (SLM) of metallic powder, Int. J. Adv. Manuf. Technol. 87 (2016) 647–656, https://doi.org/10.1007/s00170-016-8466-y.

[30] B. Clausen, C.R. D`Elia, M.B. Prime, M.R. Hill, J.E. Bishop, K.L. Johnson, B. H. Jared, K.M. Allen, D.K. Balch, R.A. Roach, D.W. Brown, Complementary Measurements of Residual Stresses Before and After Base Plate Removal in an Intricate Additively-Manufactured Stainless-Steel Valve Housing, Addit. Manuf. 36 (2020) 101555, https://doi.org/10.1016/j.addma.2020.101555.

[31] S. Lv, H. Tao, Y. Hong, Y. Zheng, C. Zhou, J. Zheng, L. Zhang, Surface treatment and corrosion behavior of 316L stainless steel fabricated by selective laser melting, Mater. Res. Express 6 (2019), https://doi.org/10.1088/2053-1591/ab3570.

[32] A.M. Philip, K. Chakraborty, Some studies on the machining behaviour of 316L austenitic stainless steel, Mater. Today:. Proc. 56 (2022) 681–685, https://doi.org/10.1016/j.matpr.2022.01.132.

[33] A. Riemer, S. Leuders, M. Thöne, H.A. Richard, T. Tröster, T. Niendorf, On the fatigue crack growth behavior in 316L stainless steel manufactured by selective laser melting, Eng. Fract. Mech. 120 (2014) 15–25, https://doi.org/10.1016/j.engfracmech.2014.03.008.

[34] B. Blinn, F. Krebs, M. Ley, R. Teutsch, T. Beck, Determination of the influence of a stress-relief heat treatment and additively manufactured surface on the fatigue behavior of selectively laser melted AISI 316L by using efficient short-time procedures, Int. J. Fatigue 131 (2020), https://doi.org/10.1016/j.ijfatigue.2019.105301.

[35] M. Braun, E. Mayer, I. Kryukov, C. Wolf, S. Böhm, A. Taghipour, R.E. Wu, S. Ehlers, S. Sheikhi, Fatigue strength of PBF-LB/M and wrought 316L stainless steel: effect of post-treatment and cyclic mean stress, Fatigue Fract. Eng. M 44 (2021) 3077–3093, https://doi.org/10.1111/ffe.13552.

[36] S. Han, T.D. Dinh, I. De Baere, M. Boone, I. Josipovic, W. Van Paepegem, Study of the effect of defects on fatigue life prediction of additive manufactured Ti-6Al-4V by combined use of micro-computed tomography and fracture-mechanics-based simulation, Int. J. Fatigue 180 (2024), https://doi.org/10.1016/j.ijfatigue.2023.108110.

[37] M.L. Montero-Sistiaga, M. Godino-Martinez, K. Boschmans, J.-P. Kruth, J. Van Humbeeck, K. Vanmeensel, Microstructure evolution of 316L produced by HP-SLM (high power selective laser melting), Addit. Manuf. 23 (2018) 402–410.

[38] J. Fu, H. Li, X. Song, M. Fu, Multi-scale defects in powder-based additively manufactured metals and alloys, J. Mater. Sci. Technol. (2022).

[39] O. Gokcekaya, T. Ishimoto, S. Hibino, J. Yasutomi, T. Narushima, T. Nakano, Unique crystallographic texture formation in Inconel 718 by laser powder bed fusion and its effect on mechanical anisotropy, Acta Materialia 212 (2021) 116876.

[40] M. Ghayoor, K. Lee, Y. He, C.-H. Chang, B.K. Paul, S. Pasebani, Selective laser melting of 304L stainless steel: Role of volumetric energy density on the microstructure, texture and mechanical properties, Addit. Manuf. 32 (2020) 101011.

[41] A. Mostafaei, C. Zhao, Y. He, S. Reza Ghiaasiaan, B. Shi, S. Shao, N. Shamsaei, Z. Wu, N. Kouraytem, T. Sun, J. Pauza, J.V. Gordon, B. Webler, N.D. Parab, M. Asherloo, Q. Guo, L. Chen, A.D. Rollett, Defects and anomalies in powder bed fusion metal additive manufacturing. Curr. Opin. Solid State Mater. Sci., 26 (2022). https://doi.org/10.1016/j.cossms.2021.100974.

[42] Z. Wang, T.A. Palmer, A.M. Beese, Effect of processing parameters on microstructure and tensile properties of austenitic stainless steel 304L made by directed energy deposition additive manufacturing, Acta Materialia 110 (2016) 226–235, https://doi.org/10.1016/j.actamat.2016.03.019.

[43] A. Taghipour, Y. Mazaheri, J. McDavid, S. Sheikhi, M. Braun, J. Shen, B. Klusemann, S. Ehlers, Strengthening Mechanisms and Strain Hardening Behavior of 316L Stainless Steel Manufactured by Laser-Based Powder Bed Fusion, Adv. Eng. Mater. 25 (2022), https://doi.org/10.1002/adem.202201230.

[44] J. Gordon, C. Haden, H. Nied, R. Vinci, D. Harlow, Fatigue crack growth anisotropy, texture and residual stress in austenitic steel made by wire and arc additive manufacturing, Mater. Sci. Eng. A 724 (2018) 431–438.

[45] A. Sarmast, J. Schubnell, J. Preußner, M. Hinterstein, E. Carl, Residual stress analysis in industrial parts: a comprehensive comparison of XRD methods, J. Mater. Sci. 58 (2023) 16905–16929, https://doi.org/10.1007/s10853-023-09069-z.

[46] D. Sikarskie, A series form of correction to stresses measured using X-Ray diffraction, AIME Met Soc Trans 239 (1967) 577–580.

[47] M. Sanchez-Poncela, S. Cabeza, J.M. Martinez, A. Cabrera, R. Rementeria, Microstructural and neutron residual stress characterization of 316L laser-powder bed fusion simplified end-use part: A modelling benchmark, Mater. Des. 237 (2024), https://doi.org/10.1016/j.matdes.2023.112526.

[48] M. Braun, C. Fischer, J. Baumgartner, M. Hecht, I. Varfolomeev, Fatigue crack initiation and propagation relation at notched specimens with welded joint characteristics, Metals 12 (2022), https://doi.org/10.3390/met12040615.

[49] ASTM E647-15e1, Standard Test Method for Measurement of Fatigue Crack Growth Rates. West Conshohocken, PA, (2015).

[50] M. Benedetti, C. Santus, Notch fatigue and crack growth resistance of Ti-6Al-4V ELI additively manufactured via selective laser melting: A critical distance approach to defect sensitivity, Int. J. Fatigue 121 (2019) 281–292, https://doi.org/10.1016/j.ijfatigue.2018.12.020.

[51] M. Benedetti, M. Dallago, C. Santus, Statistical significance of notch fatigue prognoses based on the strain-energy–density method: Application to conventionally and additively manufactured materials, Theor. Appl. Fract. Mech. 109 (2020), https://doi.org/10.1016/j.tafmec.2020.102720.

[52] C.E. Stromeyer, W.E. Dalby, The determination of fatigue limits under alternating stress conditions. Proceedings of the Royal Society of London. Series A, Containing Papers of a Mathematical and Physical Character, 90 (1914) 411-425. https://doi.org/10.1098/rspa.1914.0066.

[53] J.E. Spindel, E. Haibach, The method of maximum likelihood applied to the statistical analysis of fatigue data, Int. J. Fatigue 1 (1979) 81–88, https://doi.org/10.1016/0142-1123(79)90012-4.

[54] K. Störzel, J. Baumgartner, Statistical evaluation of fatigue tests using maximum likelihood, Mater. Test. 63 (2021) 714–720, https://doi.org/10.1515/mt-2020-0116.